Mechanical constraints to cell cycle progression in a pseurostratified epithelium

Sophie Hecht, Gantas Perez-Mockus, Dominik Schienstock, Carles Recasens-Alvarez, Sara Merino-Aceituno, Matt Smith, Guillaume Salbreux, Pierre Degond, Jean-Paul Vincent

MECHANICAL CONSTRAINTS TO CELL CYCLE PROGRESSION IN A PSEUDOSTRATIFIED EPITHELIUM

Sophie Hecht[1,2,3]*, Gantas Perez-Mockus[1]*, Dominik Schienstock[1], Carles Recasens-Alvarez[1], Sara Merino-Aceituno[4], Matt Smith[1], Guillaume Salbreux[1,5], Pierre Degond[2,6@], and Jean-Paul Vincent[1@]

* Equivalent contribution
[@] Equivalent senior authors for correspondence

[1] The Francis Crick Institute, London NW1 1AT, UK
[2] Imperial College London, Department of Mathematics, SW7 2AZ London, UK.
[3] Present address : Sorbonne Université, CNRS, Laboratoire Jacques-Louis Lions, 75005, Paris, France
[4] University of Vienna, Faculty of Mathematics, Oskar-Morgenstern-Platz 1, 1090 Wien, Austria & University of Sussex, Department of Mathematics, Falmer BN1 9RH, UK.
[5] Present address: Department of Genetics and Evolution, University of Geneva, Quai Ernest-Ansermet 30, 1205 Geneva, Switzerland.
[6] Present address: Institut de Mathématiques de Toulouse ; UMR5219 Université de Toulouse ; CNRS UPS, F-31062 Toulouse Cedex 9, France

Lead contact: Jean-Paul Vincent (jp.vincent@crick.ac.uk)

Address correspondence to: Jean-Paul Vincent (jp.vincent@crick.ac.uk) or Pierre Degond (p.degond@imperial.ac.uk).

Twitter: @jpvincentlab

SUMMARY

As organs and tissues approach their normal size during development or regeneration, growth slows down, and cell proliferation progressively comes to a halt. Among the various processes suggested to contribute to growth termination [1-10], mechanical feedback, perhaps via adherens junctions, has been suggested to play a role [11-14]. However, since adherens junctions are only present in a narrow plane in the subapical region, other structures are likely needed to sense mechanical stresses along the apical-basal (A-B) axis, especially in a thick pseudostratified epithelium. This could be achieved by nuclei, which have been implicated in mechano-transduction in tissue culture [15]. In addition, mechanical constraints imposed by nuclear crowding and spatial confinement could affect interkinetic nuclear migration (IKNM) [16], which allows G2 nuclei to reach the apical surface, where they normally undergo mitosis [17-25]. To explore how mechanical constraints affects IKNM we devised an individual-based model that treats nuclei as deformable objects constrained by the cell cortex and the presence of other nuclei. The model predicts changes in the proportion of cell cycle phases during growth, which we validate with the cell cycle phase reporter FUCCI [26]. However, this model

does not preclude indefinite growth, leading us to postulate that nuclei must migrate basally in order to access a putative basal signal required for S-phase entry. With this refinement, our updated model accounts for the observed progressive slowing down of growth and explains how pseudostratified epithelia reach a stereotypical thickness upon completion of growth.

Keywords: Interkinetic nuclear migration, pseudostratified epithelium, proliferation control

RESULTS AND DISCUSSION

Nuclear arrangement in Drosophila wing imaginal discs

To evaluate the constraints that nuclei experience during the growth of a pseudostratified epithelium, we first performed detailed morphometric analysis of wing imaginal discs of Drosophila, epithelial structures that are set aside in the embryo [27] before undergoing massive growth during larval stages [28]. We quantified the positions and morphological features of several thousand nuclei, using anti-laminB as a marker, in cleared wing imaginal discs at 72h, 96h, and 120h after egg laying (AEL) (Figure 1 A; Figure S1A, B; Materials and Methods). This showed that, with age, nuclei occupy an increasingly thicker span of the apical-basal (A-B) axis, with 75% of nuclei spread over 10 μm at 72h AEL, 15 μm at 96h AEL, and 20 μm at 120h AEL (Figure S1C, D). Therefore, the epithelium grows in thickness as well as in surface area, as shown also by Mao and colleagues [16]. This is accompanied by increased nuclear crowding, as quantified by the proportion of space surrounding individual nuclei that is occupied by other nuclei (Figure 1B; Figure S1E). We also observed that nuclei became more rounded (quantified by V/l_{max}, the ratio between volume and largest dimension) between 96h and 116h, though not during the earlier 72h - 96h period (Figure S1F). Therefore, our morphometric analysis, and the work of Kirkland et al [16], suggest that nuclei find themselves in an evolving mechanical environment during disc growth. We next investigated *in silico* how this could impact IKNM and hence cell cycle progression.

Modelling Interkinetic nuclear migration

We opted for an individual-based model to describe dividing nuclei in a confined space because it allowed us to readily incorporate established features of cell cycle progression in a pseudo-stratified epithelium. Since it is challenging to model 3D deformable objects, we decided to represent nuclei as 2D objects evolving within a 2D elastic box (Figure 1C and Methods S1). To account for deformability, nuclei were modelled as 20-sided polygons with variable angles and side lengths. In real life, nuclei are confined within the cell membrane,

which, in pseudostratified epithelia, maintains a connection to both the apical and basal surfaces, thus preventing nuclei from straying too far laterally. The cell membrane and associated cortex are also expected to exert a squeezing force orthogonal to the A-B axis. These effects were modelled with an energy that minimises the distance between a virtual apical-to-basal cable and all the polygon's vertices (Figure 1D). This will be referred to as the cable-to-nuclei energy. The basal anchor of each cable was allowed to move along the basal surface to allow nuclei to move past each other more easily. To calculate the total energy of the system, we considered three features, the elasticity of the box, the deformation of all the nuclei, and the cable-to-nuclei energy. Additional constraints were introduced 1) to prevent nuclei from overlapping with each other or with the box, 2) to ensure surface area conservation and nuclear convexity, and 3) to limit excessive deformation and movement of the box. These energies and constraints allowed us to formally define a minimisation problem (see Methods S1). Thus, at any time t, the shape of the box and the location and shape of the nuclei are a solution of this minimisation problem; the system is at a minimal energy state and fulfils all constraints. This state was then disrupted by the growth and movement of individual nuclei and a new minimisation cycle was used to compute the next equilibrium at time t+dt (Figure 1E).

We next incorporated specific assumptions to account for the activities known to be associated with various phases of the cell cycle (Figure 1F). In pseudostratified epithelia, nuclei must migrate to the apical surface to undergo mitosis. The mechanistic basis of this requirement is unclear [17,20,29], but it is considered to be an essential feature of cell cycle progression in pseudostratified epithelia (assumption A1). In accordance with previous findings [21,22,25,30-32], we assume that the apical-ward movement of G2 nuclei is an active process, probably driven by actomyosin [21,22]. This was implemented by two forces: First, we introduced a spring connecting the centre of mass of the nucleus to the apical anchor point of the cable to the apical surface. The rest length of this spring was set to zero, but with the pulling force inactivated as soon as the edge of the nucleus reaches the apical surface. The second force is governed by a gradient flow energy (see Methods S1) that prevents large movements of nuclei in a single iteration. Since live imaging suggests the existence of a narrow apical region where only mitotic nuclei can enter [20,21], we incorporated in the model an apical zone that repels non-mitotic nuclei. (See Methods S1). In vivo, as nuclei enter this zone, they round up [33-35], a process that we implemented by inactivating the cable-to-nuclei energy. Upon completion of nuclear division, a new cell membrane must be generated. In

some cases, this is achieved by equal division of the mother cell membrane [36]. However, it is also observed that one daughter cell maintains the apical and basal connections of the mother while the other daughter grows new extensions that reach the apical and basal surface of the epithelium [23,37]. We have implemented a similar activity in our simulation by allowing one of the daughters (chosen randomly) to re-establish contacts within 6 or 12 minutes after mitosis (see Methods S1). As soon as anchor points are re-established, nuclei are allowed to commence their basal-ward descent, which we considered to be passive, under the influence of other nuclei [25,30,38] (assumption A2). Following mitosis, nuclear volume must obviously grow before another mitosis takes place. Work with cultured cells has suggested that nuclear re-growth can occur during G1 and S [39-41]. Here, for simplicity, we specified that nuclei double in volume during S phase only (assumption A3). We now consider the duration of cell cycle phases. In our initial set of simulations, the duration of S and G1 were specified a priori, with that of G2 being an output of the model. Based on previous estimates [42] (see Methods S1), we set S phase to last 8h+/-2h, while G1 was set to last from 2h at the onset of the simulation (to mimic the situation in young discs) to 10 hours at the end (as observed in old discs) [42] (assumption A4). In subsequent simulations (described in the section entitled 'A basal signal could impose a second gate to cell cycle progression') neither G2 nor G1 were preassigned.

The model predicts that crowding affects IKNM and cell cycle progression

To initiate simulations with the above assumptions, the box was seeded with 10 nuclei, seven in G1 (red), three in S (blue), and none in G2 (magenta), in accordance with ratios measured in young imaginal discs [42]. Snapshots at different times (Figures 2A and S2A, see full simulation in Video S1) suggest that, as time progresses, the number of nuclear layers, the thickness of the region occupied by nuclei, and nuclear crowding increase. This was confirmed by quantifying the output of 20 simulations, as illustrated in Figures 2B-C and S2B-C (see details in Methods). Therefore, our simulations recapitulate the key features of nuclear morphology and organisation observed in fixed imaginal discs, providing support for the basic tenets of our model, and allowing us to make predictions about nuclear behaviour during proliferation.

One prediction of the model is that the apical-ward motion of G2 nuclei would slow down as the environment becomes increasingly crowded. Indeed, we found that the motion of virtual G2 nuclei during the hour preceding mitosis was on average 1.5-fold slower at the end of

simulations than at the beginning (Figures 2D and S2D). As a consequence, G2 nuclei are predicted to need an increasing amount of time to reach the apical surface and being allowed to undergo mitosis (Figures 2E and S2E). Our simulations also predict that, with 'tissue age', an increasing number of G2 nuclei may not reach the apical surface within the duration of the simulation (Figures 2F and S2F), thus being unable to complete the cell cycle. As G2 lengthen, the proportion of G2 nuclei is expected to rise. Indeed, our simulations compute this parameter to be 17.9% at the beginning and 40.7% at the end. Interestingly, this increase was accompanied with a reduction in the computed proportion of S phase nuclei (Figures 2G and S2G) and a slowing down of the growth rate. The model also predicts a change in the spatial distribution of G2 nuclei, with a progressive accumulation in the middle of the A-B axis as the simulations progress (Figures 2H and S2H). In summary, our simulations make predictions about the rate of apical-ward movement of G2 nuclei, the duration of the G2 phase, the percentage of G2 and S nuclei and the spatial distribution of G2 nuclei.

Comparing the distribution of cell cycle stages in vivo and in silico

We now evaluate to what extent the predictions of our model are borne out by *in vivo* observations. The apical-ward velocity of G2 nuclei during IKNM was experimentally measured recently and found to decrease with age [16]. And a second prediction of our model, the increasing duration of G2 during imaginal disc growth was inferred from measurements of EDU incorporation at different stages (compare Figure 2E-F to Figure S6D in [42] and to Figure 2D in [43]). To assess the remaining two predictions, we used FUCCI, which allows determination of cell cycle phases [26] (Figure 3A). A FUCCI-encoding transgene was included in the imaginal discs used for the earlier morphometric analysis, as illustrated in Figure 3B and Figure S3A. The proportion of nuclei in G2 was found to increase from 19.2% at 72h AEL to 53.2% at 116h AEL (Figure 3C and Figure S3B). During the same period, the proportion of nuclei in S decreased 2.1-fold while that of G1 nuclei remained constant at about 24.9 % of the total number. These observations match qualitatively with the prediction of the model. We then turned to the distribution of cell cycle phases along the A-B axis (Figure 3D and figure S3C). To this end, we divided the tissue along the A-B axis in 5 μm deep bins and counted the proportion of the three cell cycle phases for all the nuclei within each bin. As expected from the fact that mitosis takes place only at the apical surface, there was an excess of G1 nuclei and a dearth of G2 nuclei in the most apical bins (both 96h and 116h). The overall increase in the proportion of G2 nuclei was particularly noticeable in the

middle of the A-B axis, in accordance with our simulations. In the simulations, the A-B distributions of G2 and G1 nuclei did not match, as they do in vivo. Nevertheless, the simulations qualitatively recapitulated several in vivo observations, including the increases in nuclear layers and crowding, the changes in proportions of nuclei in the different cell cycle phases, the lengthening of the G2 phase duration and the reduction in the terminal G2 speed.

A basal signal could impose a second gate to cell cycle progression

According to our model, nuclei progressively undergo cell cycle arrest as they become increasingly unable to reach the apical surface. However, if apical localisation was the only gate to cell cycle progression, apical nuclei would be expected to proliferate indefinitely. Since this is not observed *in vivo*, we hypothesise that an additional signal controls cell cycle progression. For example, one could envision that a basal signal is required for S-phase entry, forcing nuclei to move basally if they are to continue cycling. Although hypothetical, the existence of a basal signal is not without precedent since basal Wnt5 has recently been show to control IKNM in the small intestine of the mouse [44]. Moreover, since the basal surface of wing imaginal discs is facing the circulation, a basal signal could mediate systemic control of cell cycle progression, allowing tissue intrinsic and extrinsic influences to be integrated. We formalised the requirement for a basal signal by modifying assumption A4 (Figure 4A and Methods S1). In this framework, the duration of G1 no longer needs to be specified *a priori*. Nevertheless, the model was still able to recapitulate all the experimentally observed features, including the proportion of cell cycle phases observed over time in vivo (Figure 4B; Figure S4A-E). In addition, the refined model confirmed the expectation that increasing the range of the basal signal would lead to a larger number of nuclear layers (Figure 4C; Figure S4F; Video S2 to S4), perhaps by allowing nuclei to enter S-phase more rapidly (Figure S4G).

Conclusion

Here we have taken a computational approach to investigate how mechanical constraints could impact on IKNM and hence proliferation in a pseudostratified epithelium. Previous models of nuclear mechanics within tissues have either taken a macroscopic view ([38,45,46]) or have considered a microscopic view without allowing nuclear deformation ([24,47]). By representing nuclei as 20-sided polygon, we were able to infer their deformability, compute the forces that impact their movement, and thus build a mechanical model of IKNM. Our model was able to reproduce experimentally observed features of growing wing imaginal discs, including progressive nuclear layering, the distribution of cell cycle phases across the

A-B axis, the accumulation of G2 nuclei with time. It also confirmed earlier suggestions that "congestion" [48], "traffic bottleneck"[23] or nuclear density [16] affect the apical-ward component of IKNM. Crowding is also expected to impede basal-ward movement, which is needed to make space for incoming G2 nuclei and also, possibly to allow G1 nuclei to access a basal signal needed for S-phase entry. Such a signal remains hypothetical but the need for nuclei to sample both the apical and basal regions for cell cycle progression would explain why IKNM is such a common feature of developing epithelia [25,30]. Our study adds nuclear crowding to the list of processes that could contribute to growth deceleration in developing tissues, besides nutrient access, dwindling growth factor signalling, changes in hormonal control [2,9,49], and/or mechanical feedback through adherens junctions. It remains a challenge to figure out how these processes are genetically controlled and integrated to ensure reproducible tissue size in a wide variety of conditions.

ACKNOWLEDGEMENTS

This work was supported by core funding to the Francis Crick Institute (FC001204 to JPV and FC001317 to G.S.), a Wellcome Trust Investigator award (206341/Z/17/Z to JPV), by the Engineering and Physical Sciences Research Council (EP/M006883/1 to PD), by the Royal Society and the Wolfson Foundation through a Royal Society Wolfson Research Merit Award (WM130048 to PD) and by the National Science Foundation (RNMS11-07444 (KI-Net) to PD). SH was supported by a joint Imperial College - Francis Crick Institute PhD studentship. DS was supported by a Francis Crick PhD fellowship. GPM is the recipient of a postdoctoral fellowship from EMBO (ALTF 238-2018). SMA is supported by the Vienna Science and Technology Fund (WWTF) with a Vienna Research Groups for Young Investigators grant VRG17-014.

AUTHOR CONTRIBUTIONS

This project was conceived and further elaborated by DS, SH, PD, GPM and JPV. DS devised and performed the initial morphometric analysis of fixed imaginal discs, with subsequent improvement by GPM, who also performed statistical analysis. MS and GS contributed to the segmentation pipeline. SH wrote the code and implemented the model under the supervision of PD. CR performed initial FUCCI analysis, with subsequent improvement by GPM. The model was iteratively elaborated by SH and GPM with contributions from the other authors. GPM wrote the first draft, which was subsequently modified and edited by all the authors.

DECLARATION OF INTERESTS

The authors declare no competing or financial interests.

MAIN FIGURE LEGENDS

Figure 1: Simulating interkinetic nuclear migration (IKNM) in a confined space

(**A)** Optical cross-section of the wing discs shown in Figure S1A. Individual segmented nuclei have been colored randomly. Scale bars represent 50 μm. (**B)** Distribution of crowding indices in 72h, 96h and 116h AEL wing discs (Nuclei located at the border of the segmented area were excluded; see Material and Methods for more details. 72h AEL: 4 discs, 490 nuclei. 96h AEL: 4 discs, 1968 nuclei. 116h AEL: 3 discs: 5221 nuclei). Wilcoxon rank-sum statistic test for two samples was performed in D and H. ** P<0.01 *** P<0.001.
(C) Overview of the model's main elements. The edges of the disc (including the apical and basal surfaces) are represented by an elastic box and the nuclei by polygons. The natural curvature of imaginal discs, as seen on Fig 1B, was ignored for simplicity. The energies and constraints of the model are listed. **(D)** Nuclei were represented as 20-sided deformable polygons, allowing a realistic representation, while limiting computational costs. The constraining effect of the cell cortex was represented by a cable tethered to the apical and basal sides. **(E)** Iterative progression from one minimal energy state (at time t) to the next (at time t+dt). **(F)** Behaviour of nuclei during the different phases of the cell cycle. Unless stated differently, the duration of the S and G1 phases was defined *a priori* whereas the duration of G2 was an output of the model. **See also Figure S1.**

Figure 2: In *silico*, crowding perturbs interkinetic nuclear migration and affects the distribution off cell cycle phases

(A) Snapshots of a simulation at 72h, 96h, and 116 h AEL. Nuclei were coloured according to the cell-cycle phase: G1 in red, S in blue and G2 in magenta. A yellow ribbon represents the mitotic zone where non-mitotic nuclei are excluded. **(B)** Distribution of nuclei along the apical-basal axis (expressed in units of a spherical G1 nucleus diameter, G1∅) **(C)** Distribution of computed crowding indices at different ages **(s**ee Sup. Exp. Pro. Annex 1) for 20 simulations. With time, nuclei occupy deeper positions, form more layers, and become increasingly crowded. **(D)** Terminal velocity (G1∅/h) of migrating G1 nuclei one hour

before division. This decreases as the disc 'ages'. The red curve represents a polynomial fit to the data. **(E)** Temporal evolution of G2 duration extracted from 20 simulations; a 6.5-fold increase is seen. After 90h hours, G2 duration plateaued to a value of 19 h, correlating with an increase in the cumulative number of G2 nuclei that never exit G2 ('G2 – arrested') **(F)**. Cumulative number of G2 – arrested nuclei (binned in 12h intervals). **(G)** Percentage of nuclei in G1, S and G2 (averaged from 20 simulations). The proportion of G1 nuclei increases at the expense of that of nuclei in S. **(H)** Distribution of nuclei in G1, S and G2 along the apical-basal axis at 12 hour intervals (± 6 hours). Nuclei were binned in slices of ½ G1∅ and the number of nuclei in each bin was normalised to the total number of nuclei. **See also Figure S2 and Video S1.**

Figure 3: Spatio-temporal distribution of cell cycle phases in Drosophila wing imaginal discs

(A) Schematic representation of the FUCCI system coupled with a Lamin B staining. Nuclei in G1, late S and G2 appear in red, blue, and magenta (respectively). There is no FUCCI staining in early S, while lamin B is not detectable at M. In the following analysis, early and late S nuclei were pooled together **(B)** Optical cross-section of 72h, 96h and 116h AEL wing discs expressing E2F1-RFP and CycB-GFP (same preparation as those shown in Fig. 1). **(C)** Percentage of nuclei in G1, S and G2 at different stages. Note the increase of G2 nuclei and increase of S nuclei, as predicted by the model. The same discs as those used to generate Figure 1A, B and Figure S1 were used (72h AEL: 4 discs, 836 nuclei. 96h AEL: 4 discs, 2562 nuclei. 116h AEL: 3 discs: 5889 nuclei). Error bars represent standard deviation. **(D)** Distribution of nuclei along the apical-basal axis (μm). Nuclei in each of phases were counted in slices of 5 μm (half the average spherical diameter of G1 nuclei) and normalised over the total number of nuclei.-The relative increase of G2 nuclei at late stages is consistent with 'congestion' impairing apical-ward movement. Each dot is an average from 4 discs (72h, and 96h AEL) or 3 discs (116h AEL). Panel C and D were generated from the same dataset. Error bars represent standard deviation. Scale bars represent 50 μm. **See also Figure S3.**

Figure 4: A two-gate model of IKNM: A basal signal could regulate nuclear layering, crowding and proliferation rates

(A) Modification of the model to include a hypothetical basal signal that triggers the G1-S transition. Only the duration of S is defined *a priori* by the model, whereas the duration of G1 and G2 are outputs. The range of this signal (λ) was expressed in multiples of G1 nuclear diameters (see Sup. Exp. Pro. Annex 1 for more details). **(B)** Simulations with λ=10 nuclear diameters recapitulated the increase of G2 percentage that occurs as the tissue grows. **(C)** Snapshots of simulation output at 116h AEL with λ=2, λ=4 or λ=10). G1 nuclei are coloured in red, S in blue and G2 in magenta. A yellow ribbon represents the mitotic zone where non-mitotic nuclei are excluded. **See also Figure S4, and Video** S2-4.

STAR METHODS

RESOURCE AVAILABILITY

Lead contact.

Further information and requests for resources and reagents should be directed to and will be fulfilled by the Lead Contact, Jean-Paul Vincent (jp.vincent@crick.ac.uk).

Materials Availability Statements.

This study did not generate new unique reagents.

Data and Code Availability.

* All data reported in this paper will be shared by the lead contact upon request.
* All original code has been deposited at https://zenodo.org/record/6190050#.YhPPxi2ZPdR and is publicly available as of the date of the publication. DOIS are listed in the key resource table.
* Any additional information required to reanalyse the data reported in this work paper is available from the Lead Contact upon request.

EXPERIMENTAL MODEL AND SUBJECT DETAIL

The only experimental model used in this study is *Drosophila melanogaster*. No regulatory approval is needed for this species. Relevant information on the crosses, genotypes and husbandry are indicated in the Methods Details.

METHODS DETAILS

Fly stocks and husbandry

Flies were reared in standard cornmeal/agar media at 25C. Larvae were staged from the time of L2-L3 transition. The following strains were obtained from the Bloomington stock center: *nubbin-Gal4*, *UAS-FUCCI* (UAS-GFP.E2f1.1-230, UAS-mRFP1.NLS.CycB.1-266 on the III) and *pdm2^{R11F02}*-Gal4.

Genotypes

Figure 1A, B, Figure 3B-D, Figure S1, Figure S3: the same dataset of 11 discs was used in these figure panels. For the 96h and 116h AEL wing discs, the genotype was *nubbin-Gal4/UAS-FUCCI* and for the 72h AEL wing discs, it was *pdm2^{R11F02}*-Gal4*/UAS-FUCCI*. *Pdm2^{R11F02}*-Gal4 is a pouch marker which is stronger at 72h AEL than *nubbin-gal4* [50].
Figure S1B: *tub-G4*/*UAS-CD8-GFP*

Immunohistochemistry and imaging

Wing imaginal discs were fixed in 4% formaldehyde for 40 min using standard procedures. The discs were then incubated overnight at 4^{o}C with a mixture of two anti-Lamin B (1:100, ADL67.10-s, DSHB and ADL84.12-s in PBS with TritonX at 0.5%) antibodies, followed by two hours in anti-mouse Alexa Fluor Plus 647 (1:1000, A32728, Invitrogen) at room temperature. To preserve 3D structure, the fixed and stained discs were deposited in warm low melting agar (1% low melting point agar (A9414 Sigma- Aldrich) in PBS). 10µl of liquid agar containing the wing disc was then transferred onto a 1.5x coverslip. Before solidification of the agar, the wing disc was positioned at the bottom of the drop, with the pouch area facing down. The drop was surrounded with a ring of silicone grease (Z273544 Aldrich), creating a small chamber. 10µl of FocusClear^{TM} (FC-101, 2Bscientific) was then added on top of the agar drop and allowed to act for 1h in a dark humid chamber. Subsequently, FocusClear^{TM} was removed and 20µl of MountClear^{TM} (MC-301, 2Bscientific) was added. A slide was then positioned on top of the grease to close the chamber. The slide was then inverted, and the discs were imaged with an upright Leica SP5 confocal microscope equipped with a 63x glycerol (1.3 NA) objective, with a pixel size of 0.24 x 0.24 µm and a z step of 0.7 µm.

Image analysis

Before segmentation, the region of interest was manually cropped using FIJI [51]. For eight of the eleven discs analysed, nuclei were segmented using the Nessys module of PickCells [52]. For

the 3 remaining discs a machine learning algorithm (see below) was used to generate a binary mask of the segmented nuclei. This binary mask was then fed into Nessys to segment individual nuclei.

Nessys then calculated the center of mass, volume, length of the longest axis (l_{max}) as well as the mean fluorescence values in the different channels (E2F1 and CycB) inside each segmented nuclei.

To rotate the sample, a custom-made python code using the Numpy and Scikit-image libraries was used to define a plane based on three points manually picked and located in the most apical part of the disc. This plane coupled to a normal vector allowed to define a new frame-of-reference, and to re-calculate the coordinates of each of the center of mass of the nuclei.

The wing disc curvature was accounted for by first binning the nuclei in squares defined orthogonally to the apical plane. The coordinates of the most apical nucleus were then used as the reference point to recalculate the position along the z-axis (depth) of all the other nuclei present in the bin.

The cell cycle-phase was determined by comparing the binarized values of the E2F1 and CycB signals (Figure 3A). Nuclei in early or late S phase were pooled together in all the analyses and considered as S phase.

Crowding was calculated by first generating a 3D box surrounding each nuclei. This box was 30 pixels bigger than the most extreme values of the nucleus on the x and y axis and 10 pixels on the z axis. Then, after ignoring the voxels containing the nucleus of interest for the analysis, for each box, the number of voxels containing another nucleus (volume of surrounding nuclei) was divided by the total number of voxels (theoretical available volume). Nuclei located at a distance below 4 μm of the border of the segmentation area where ignored.

Machine learning for the segmentation of the nuclei

Images were processed using a modified 3D Unet [53] to create a distance transform that Nessys [52] could segment. The network produced 3 output layers: the nuclei's boundary, a mask of nuclei and background, and a distance transform of segmented images. Training labels were created using segmentation outputs from Nessys. Each labelled cell was converted into a binary mask, a binary border, and a distance transform. The distance transform was performed by eroding the binary blob that represents an individual cell. Our unet implementation using python and tensorflow source code is available online [54].

Mathematical simulations

Simulations were performed according to the model and method described in Method S1.

QUANTIFICATION AND STATISTICAL ANALYSIS

Data for the sample number (number of wing discs, nuclei or simulations), statistical significance (represented as * $p<0.05$, ** $p<0.01$, *** $p<0.001$) as well as dispersion measures (standard deviation) is given in the figures and the figures legends. All statistical tests were performed using the stats module from the SciPy python library.

A Wilcoxon signed rank sum test was used after testing for normality using a Shapiro-Wilk test. There was no blinding performed.

The graphs in Figure 1B, Figure 2H, Figure 3C, Figure S1D,F,G, Figure S2H, Figure S3 B,C and Figure S4E were performed using the python libraries Seaborn and MatplotLib. The graphs in Figure 2B-G, Figure 4B, Figure S2B-G, Figure S4A-D,F-M were performed with MATLAB.

SUPPLEMENTAL VIDEO LEGENDS

Video S1: Simulation of IKNM in a confined space. Related to Figure 2.

Video S2:Simulation of IKNM in a confined space with a basal signal range of $\lambda = 2$. Related to Figure 4.

Video S3: Simulation of IKNM in a confined space with a basal signal range of $\lambda = 4$. Related to Figure 4.

Video S4: Simulation of IKNM in a confined space with a basal signal range of $\lambda = 10$. Related to Figure 4.

In all the videos, the nuclei are colour-coded according to the cell cycle phase: G1 (red) , S (blue) and G2 (magenta). Nuclei in mitosis appear in white.

METHODS S1.

This section describes in detail the Individual-Based Models used to simulate the behaviour of nuclei in imaginal disc of Drosophila. Related to STAR Methods.

REFERENCES

1. Bryant, P.J., and Levinson, P. (1985). Intrinsic growth control in the imaginal primordia of Drosophila, and the autonomous action of a lethal mutation causing overgrowth. Dev Biol *107*, 355-363.
2. Boulan, L., Milan, M., and Leopold, P. (2015). The Systemic Control of Growth. Cold Spring Harb Perspect Biol *7*. 10.1101/cshperspect.a019117.

3. Gokhale, R.H., and Shingleton, A.W. (2015). Size control: the developmental physiology of body and organ size regulation. Wiley Interdiscip Rev Dev Biol *4*, 335-356. 10.1002/wdev.181.
4. Barrio, L., and Milan, M. (2017). Boundary Dpp promotes growth of medial and lateral regions of the Drosophila wing. Elife *6*. 10.7554/eLife.22013.
5. Vollmer, J., Casares, F., and Iber, D. (2017). Growth and size control during development. Open Biol *7*. 10.1098/rsob.170190.
6. Zecca, M., and Struhl, G. (2010). A feed-forward circuit linking wingless, fat-dachsous signaling, and the warts-hippo pathway to Drosophila wing growth. PLoS Biol *8*, e1000386. 10.1371/journal.pbio.1000386.
7. Zecca, M., and Struhl, G. (2007). Control of Drosophila wing growth by the vestigial quadrant enhancer. Development *134*, 3011-3020. 10.1242/dev.006445.
8. Zecca, M., and Struhl, G. (2007). Recruitment of cells into the Drosophila wing primordium by a feed-forward circuit of vestigial autoregulation. Development *134*, 3001-3010. 10.1242/dev.006411.
9. Harmansa, S., and Lecuit, T. (2021). Forward and feedback control mechanisms of developmental tissue growth. Cells Dev, 203750. 10.1016/j.cdev.2021.203750.
10. Hariharan, I.K. (2015). Organ Size Control: Lessons from Drosophila. Dev Cell *34*, 255-265. 10.1016/j.devcel.2015.07.012.
11. Shraiman, B.I. (2005). Mechanical feedback as a possible regulator of tissue growth. Proc Natl Acad Sci U S A *102*, 3318-3323. 10.1073/pnas.0404782102.
12. Irvine, K.D., and Shraiman, B.I. (2017). Mechanical control of growth: ideas, facts and challenges. Development *144*, 4238-4248. 10.1242/dev.151902.
13. LeGoff, L., and Lecuit, T. (2015). Mechanical Forces and Growth in Animal Tissues. Cold Spring Harb Perspect Biol *8*, a019232. 10.1101/cshperspect.a019232.
14. Pinheiro, D., and Bellaiche, Y. (2018). Mechanical Force-Driven Adherens Junction Remodeling and Epithelial Dynamics. Dev Cell *47*, 3-19. 10.1016/j.devcel.2018.09.014.
15. Buxboim, A., Swift, J., Irianto, J., Spinler, K.R., Dingal, P.C., Athirasala, A., Kao, Y.R., Cho, S., Harada, T., Shin, J.W., and Discher, D.E. (2014). Matrix elasticity regulates lamin-A,C phosphorylation and turnover with feedback to actomyosin. Curr Biol *24*, 1909-1917. 10.1016/j.cub.2014.07.001.
16. Kirkland, N.J., Yuen, A.C., Tozluoglu, M., Hui, N., Paluch, E.K., and Mao, Y. (2020). Tissue Mechanics Regulate Mitotic Nuclear Dynamics during Epithelial Development. Curr Biol *30*, 2419-2432 e2414. 10.1016/j.cub.2020.04.041.
17. Norden, C. (2017). Pseudostratified epithelia - cell biology, diversity and roles in organ formation at a glance. J Cell Sci *130*, 1859-1863. 10.1242/jcs.192997.
18. Del Bene, F. (2011). Interkinetic nuclear migration: cell cycle on the move. EMBO J *30*, 1676-1677. 10.1038/emboj.2011.114.
19. Spear, P.C., and Erickson, C.A. (2012). Interkinetic nuclear migration: a mysterious process in search of a function. Dev Growth Differ *54*, 306-316. 10.1111/j.1440-169X.2012.01342.x.
20. Lee, H.O., and Norden, C. (2013). Mechanisms controlling arrangements and movements of nuclei in pseudostratified epithelia. Trends Cell Biol *23*, 141-150. 10.1016/j.tcb.2012.11.001.
21. Meyer, E.J., Ikmi, A., and Gibson, M.C. (2011). Interkinetic nuclear migration is a broadly conserved feature of cell division in pseudostratified epithelia. Curr Biol *21*, 485-491. 10.1016/j.cub.2011.02.002.

22. Liang, L., Haug, J.S., Seidel, C.W., and Gibson, M.C. (2014). Functional genomic analysis of the periodic transcriptome in the developing Drosophila wing. Dev Cell *29*, 112-127. 10.1016/j.devcel.2014.02.018.
23. Miyata, T., Okamoto, M., Shinoda, T., and Kawaguchi, A. (2014). Interkinetic nuclear migration generates and opposes ventricular-zone crowding: insight into tissue mechanics. Front Cell Neurosci *8*, 473. 10.3389/fncel.2014.00473.
24. Ferreira, M.A., Despin-Guitard, E., Duarte, F., Degond, P., and Theveneau, E. (2019). Interkinetic nuclear movements promote apical expansion in pseudostratified epithelia at the expense of apicobasal elongation. PLoS Comput Biol *15*, e1007171. 10.1371/journal.pcbi.1007171.
25. Leung, L., Klopper, A.V., Grill, S.W., Harris, W.A., and Norden, C. (2011). Apical migration of nuclei during G2 is a prerequisite for all nuclear motion in zebrafish neuroepithelia. Development *138*, 5003-5013. 10.1242/dev.071522.
26. Zielke, N., Korzelius, J., van Straaten, M., Bender, K., Schuhknecht, G.F.P., Dutta, D., Xiang, J., and Edgar, B.A. (2014). Fly-FUCCI: A versatile tool for studying cell proliferation in complex tissues. Cell Rep *7*, 588-598. 10.1016/j.celrep.2014.03.020.
27. Requena, D., Alvarez, J.A., Gabilondo, H., Loker, R., Mann, R.S., and Estella, C. (2017). Origins and Specification of the Drosophila Wing. Curr Biol *27*, 3826-3836 e3825. 10.1016/j.cub.2017.11.023.
28. Milan, M., Campuzano, S., and Garcia-Bellido, A. (1996). Cell cycling and patterned cell proliferation in the wing primordium of Drosophila. Proc Natl Acad Sci U S A *93*, 640-645.
29. Cammarota, C.M., and Bergstralh, D. (2020). Cell Division: Interkinetic Nuclear... Mechanics. Curr Biol *30*, R759-R761. 10.1016/j.cub.2020.05.028.
30. Norden, C., Young, S., Link, B.A., and Harris, W.A. (2009). Actomyosin is the main driver of interkinetic nuclear migration in the retina. Cell *138*, 1195-1208. 10.1016/j.cell.2009.06.032.
31. Rujano, M.A., Sanchez-Pulido, L., Pennetier, C., le Dez, G., and Basto, R. (2013). The microcephaly protein Asp regulates neuroepithelium morphogenesis by controlling the spatial distribution of myosin II. Nat Cell Biol *15*, 1294-1306. 10.1038/ncb2858.
32. Yanakieva, I., Erzberger, A., Matejcic, M., Modes, C.D., and Norden, C. (2019). Cell and tissue morphology determine actin-dependent nuclear migration mechanisms in neuroepithelia. J Cell Biol *218*, 3272-3289. 10.1083/jcb.201901077.
33. Stewart, M.P., Helenius, J., Toyoda, Y., Ramanathan, S.P., Muller, D.J., and Hyman, A.A. (2011). Hydrostatic pressure and the actomyosin cortex drive mitotic cell rounding. Nature *469*, 226-230. 10.1038/nature09642.
34. Matthews, H.K., Delabre, U., Rohn, J.L., Guck, J., Kunda, P., and Baum, B. (2012). Changes in Ect2 localization couple actomyosin-dependent cell shape changes to mitotic progression. Dev Cell *23*, 371-383. 10.1016/j.devcel.2012.06.003.
35. Cadart, C., Zlotek-Zlotkiewicz, E., Le Berre, M., Piel, M., and Matthews, H.K. (2014). Exploring the function of cell shape and size during mitosis. Dev Cell *29*, 159-169. 10.1016/j.devcel.2014.04.009.
36. Kosodo, Y., Toida, K., Dubreuil, V., Alexandre, P., Schenk, J., Kiyokage, E., Attardo, A., Mora-Bermudez, F., Arii, T., Clarke, J.D., and Huttner, W.B. (2008). Cytokinesis of neuroepithelial cells can divide their basal process before anaphase. EMBO J *27*, 3151-3163. 10.1038/emboj.2008.227.
37. Kosodo, Y., and Huttner, W.B. (2009). Basal process and cell divisions of neural progenitors in the developing brain. Dev Growth Differ *51*, 251-261. 10.1111/j.1440-169X.2009.01101.x.

38. Azizi, A., Herrmann, A., Wan, Y., Buse, S.J., Keller, P.J., Goldstein, R.E., and Harris, W.A. (2020). Nuclear crowding and nonlinear diffusion during interkinetic nuclear migration in the zebrafish retina. Elife *9*. 10.7554/eLife.58635.
39. Fidorra, J., Mielke, T., Booz, J., & Feinendegen, L. E. (1981). Cellular and nuclear volume of human cells during the cell cycle. Radiation and Environmental Biophysics *19*, 205-214. 10.1007/bf01324188
40. Steen, H.B., & Lindmo, T. (1978). CELLULAR AND NUCLEAR VOLUME DURING THE CELL CYCLE OF NHIK 3025 CELLS. Cell Proliferation *11*, 69. 10.1111/j.1365-2184.1978.tb00876.x
41. Maeshima, K., Iino, H., Hihara, S., Funakoshi, T., Watanabe, A., Nishimura, M., Nakatomi, R., Yahata, K., Imamoto, F., Hashikawa, T., et al. (2010). Nuclear pore formation but not nuclear growth is governed by cyclin-dependent kinases (Cdks) during interphase. Nat Struct Mol Biol *17*, 1065-1071. 10.1038/nsmb.1878.
42. Wartlick, O., Mumcu, P., Kicheva, A., Bittig, T., Seum, C., Julicher, F., and Gonzalez-Gaitan, M. (2011). Dynamics of Dpp signaling and proliferation control. Science *331*, 1154-1159. 10.1126/science.1200037.
43. Neufeld, T.P., de la Cruz, A.F., Johnston, L.A., and Edgar, B.A. (1998). Coordination of growth and cell division in the Drosophila wing. Cell *93*, 1183-1193. 10.1016/s0092-8674(00)81462-2.
44. Wang, S., Cebrian, C., Schnell, S., and Gumucio, D.L. (2018). Radial WNT5A-Guided Post-mitotic Filopodial Pathfinding Is Critical for Midgut Tube Elongation. Dev Cell *46*, 173-188 e173. 10.1016/j.devcel.2018.06.011.
45. Postel, M., Karam, A., Pezeron, G., Schneider-Maunoury, S., and Clement, F. (2019). A multiscale mathematical model of cell dynamics during neurogenesis in the mouse cerebral cortex. BMC Bioinformatics *20*, 470. 10.1186/s12859-019-3018-8.
46. Murciano, A., Zamora, J., Lopez-Sanchez, J., and Frade, J.M. (2002). Interkinetic nuclear movement may provide spatial clues to the regulation of neurogenesis. Mol Cell Neurosci *21*, 285-300. 10.1006/mcne.2002.1174.
47. Kosodo, Y., Suetsugu, T., Suda, M., Mimori-Kiyosue, Y., Toida, K., Baba, S.A., Kimura, A., and Matsuzaki, F. (2011). Regulation of interkinetic nuclear migration by cell cycle-coupled active and passive mechanisms in the developing brain. EMBO J *30*, 1690-1704. 10.1038/emboj.2011.81.
48. Okamoto, M., Namba, T., Shinoda, T., Kondo, T., Watanabe, T., Inoue, Y., Takeuchi, K., Enomoto, Y., Ota, K., Oda, K., et al. (2013). TAG-1-assisted progenitor elongation streamlines nuclear migration to optimize subapical crowding. Nat Neurosci *16*, 1556-1566. 10.1038/nn.3525.
49. Boulan, L., and Leopold, P. (2021). What determines organ size during development and regeneration? Development *148*. 10.1242/dev.196063.
50. Boulan, L., Andersen, D., Colombani, J., Boone, E., and Leopold, P. (2019). Inter-Organ Growth Coordination Is Mediated by the Xrp1-Dilp8 Axis in Drosophila. Dev Cell *49*, 811-818 e814. 10.1016/j.devcel.2019.03.016.
51. Schindelin, J., Arganda-Carreras, I., Frise, E., Kaynig, V., Longair, M., Pietzsch, T., Preibisch, S., Rueden, C., Saalfeld, S., Schmid, B., et al. (2012). Fiji: an open-source platform for biological-image analysis. Nat Methods *9*, 676-682. 10.1038/nmeth.2019.
52. Blin, G., Sadurska, D., Portero Migueles, R., Chen, N., Watson, J.A., and Lowell, S. (2019). Nessys: A new set of tools for the automated detection of nuclei within intact tissues and dense 3D cultures. PLoS Biol *17*, e3000388. 10.1371/journal.pbio.3000388.

53. Çiçek Ö., A.A., Lienkamp S.S., Brox T., Ronneberger O (2016). 3D U-Net: Learning Dense Volumetric Segmentation from Sparse Annotation. Lecture Notes in Computer Science *9901*. 10.1007/978-3-319-46723-8_49.
54. Smith, M. Active Unet Segmentations: https://github.com/FrancisCrickInstitute/ActiveUnetSegmentation.

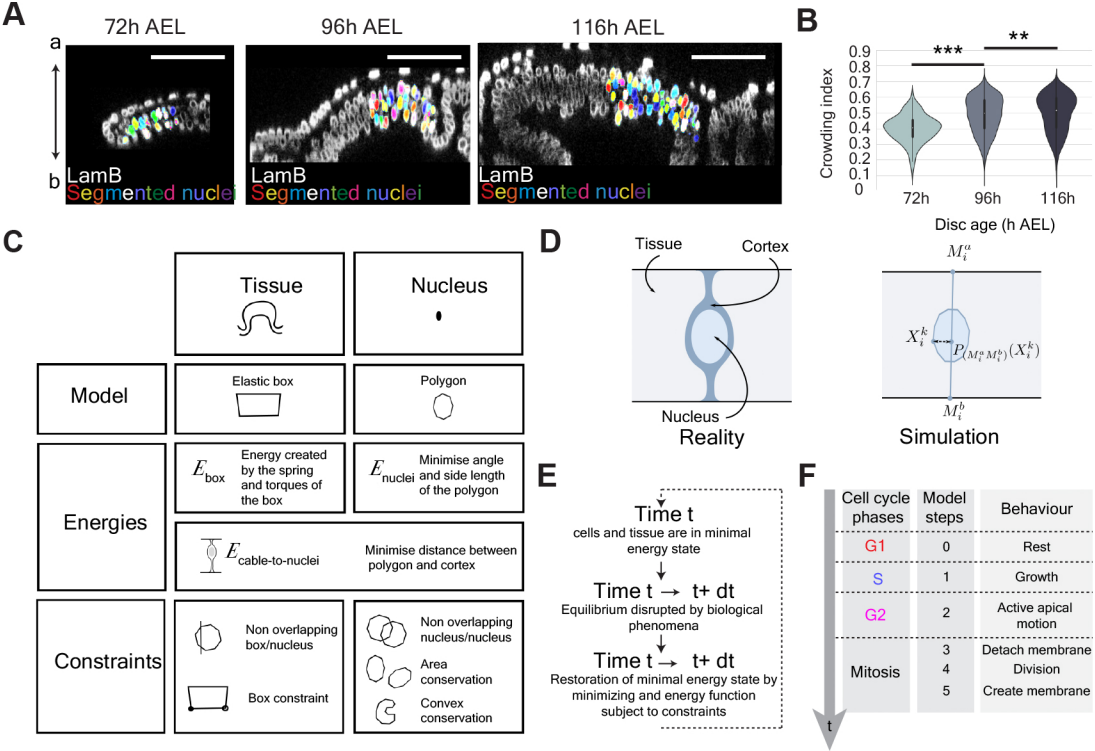
A
72h AEL
96h AEL
116h AEL
a
b
LamB
Segmented nuclei
B
Crowding index
0.9
0.8
0.7
0.6
0.5
0.4
0.3
0.2
0.1
0
***
**
72h
96h
116h
Disc age (h AEL)
C
Tissue
Nucleus
Model
Elastic box
Polygon
Energies
E_{box}
Energy created by the spring and torques of the box
E_{nuclei}
Minimise angle and side length of the polygon
$E_{cable\text{-}to\text{-}nuclei}$
Minimise distance between polygon and cortex
Constraints
Non overlapping box/nucleus
Box constraint
Non overlapping nucleus/nucleus
Area conservation
Convex conservation
D
Tissue
Cortex
Nucleus
Reality
M_i^a
X_i^k
$P_{(M_i^a M_i^b)}(X_i^k)$
M_i^b
Simulation
E
Time t
cells and tissue are in minimal energy state
Time t → t+ dt
Equilibrium disrupted by biological phenomena
Time t → t+ dt
Restoration of minimal energy state by minimizing and energy function subject to constraints
F
Cell cycle phases
Model steps
Behaviour
G1
0
Rest
S
1
Growth
G2
2
Active apical motion
Mitosis
3
Detach membrane
4
Division
5
Create membrane
t

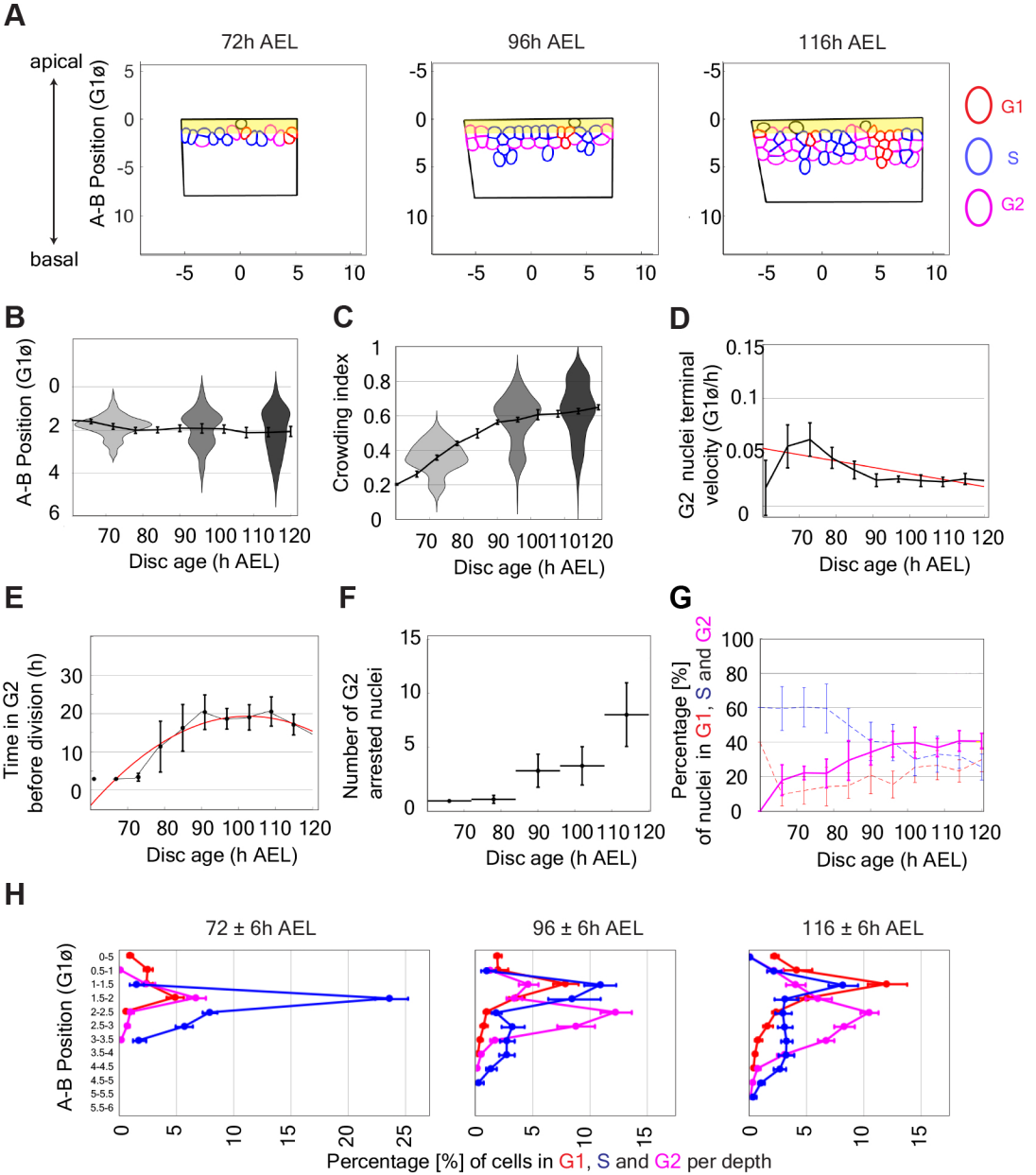
A
72h AEL
96h AEL
116h AEL
apical
basal
A-B Position (G1ø)
G1
S
G2
B
A-B Position (G1ø)
Disc age (h AEL)
C
Crowding index
Disc age (h AEL)
D
G2 nuclei terminal velocity (G1ø/h)
Disc age (h AEL)
E
Time in G2 before division (h)
Disc age (h AEL)
F
Number of G2 arrested nuclei
Disc age (h AEL)
G
Percentage [%] of nuclei in G1, S and G2
Disc age (h AEL)
H
72 ± 6h AEL
96 ± 6h AEL
116 ± 6h AEL
A-B Position (G1ø)
Percentage [%] of cells in G1, S and G2 per depth

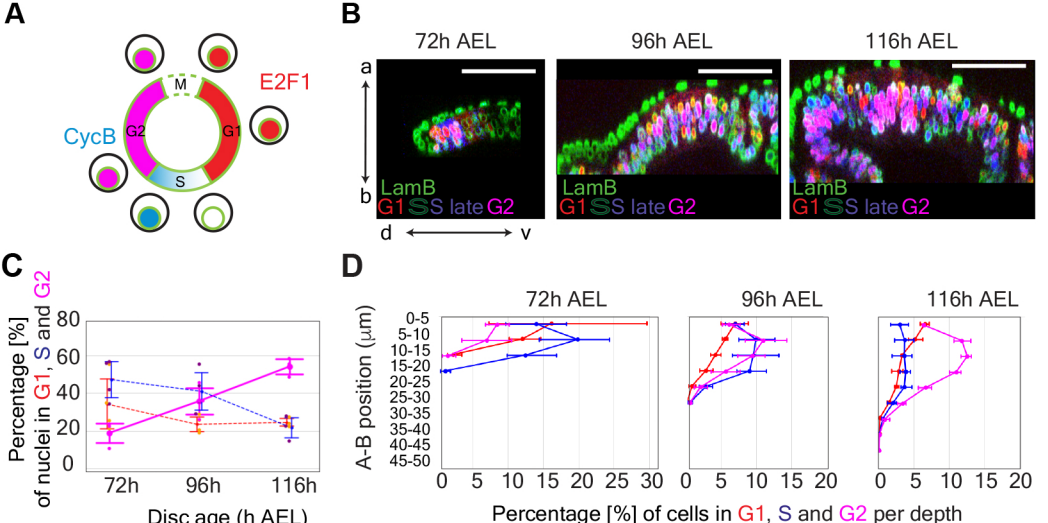
A
M
E2F1
CycB
G2
G1
S
B
72h AEL
96h AEL
116h AEL
a
b
d
v
LamB
G1 S S late G2
C
Percentage [%] of nuclei in G1, S and G2
80
60
40
20
0
72h
96h
116h
Disc age (h AEL)
D
72h AEL
96h AEL
116h AEL
A-B position (μm)
0-5
5-10
10-15
15-20
20-25
25-30
30-35
35-40
40-45
45-50
0 5 10 15 20 25 30
0 5 10 15 20
0 5 10 15 20
Percentage [%] of cells in G1, S and G2 per depth

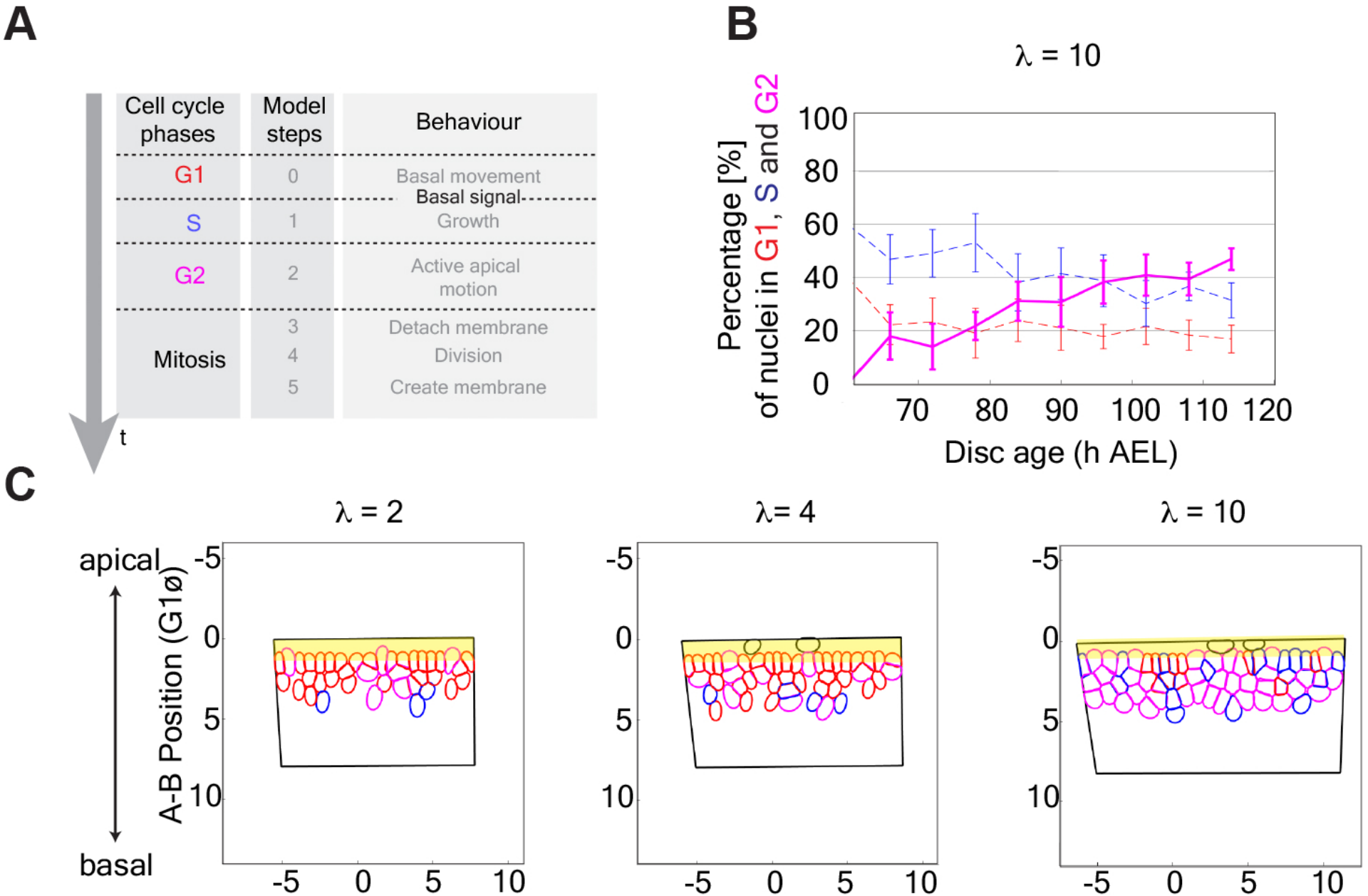
A
Cell cycle phases
Model steps
Behaviour
G1
0
Basal movement
Basal signal
S
1
Growth
G2
2
Active apical motion
Mitosis
3
Detach membrane
4
Division
5
Create membrane
t
B
λ = 10
Percentage [%] of nuclei in G1, S and G2
100
80
60
40
20
0
70
80
90
100
110
120
Disc age (h AEL)
C
λ = 2
λ= 4
λ = 10
apical
basal
A-B Position (G1ø)
-5
0
5
10

METHODS S1: NUMERICAL SIMULATIONS

In this section we describe the Individual-Based Models used for simulating the imaginal disc of Drosophila. The flowchart presented in Fig. A1 explains the structure of the model. The model is constructed such that at each time step the variables of the system are at a minimal energy state. Then at each time step the system is disrupted by biological phenomena. These phenomena are linked to the growth of the tissue and to the evolution of the nuclei, including their growth and motion during IKNM. The minimal energy state is then restored by minimising the energy functional subject to constraints. Therefore, the model was developed in an optimisation framework.

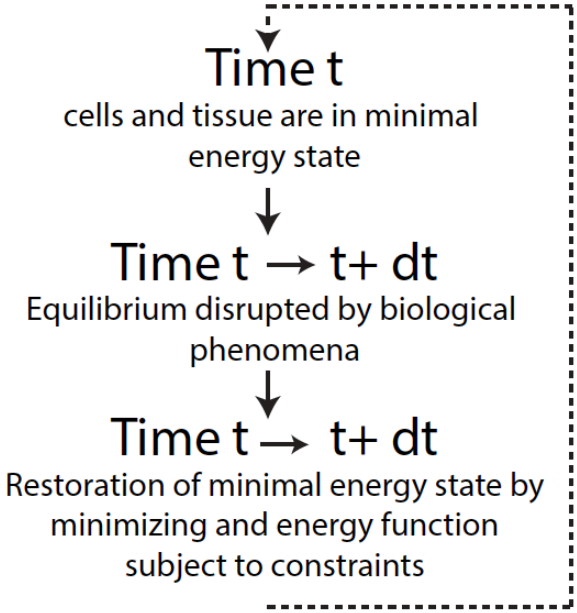

Fig. A1: Flowchart of the Individual Based Model.

We first introduce the different agents of the model, as well as the energies and constraints inherent to the biological relevance of the model with no consideration of time. Secondly, the minimisation problem is introduced, including the minimisation algorithms and the choice of the minimisation parameters. Then, a description of the time dependent part of the model is provided. Last, we present the choice of parameters.

Choice of the agents

Because the aim of the model is to study the influence of crowding on IKNM during tissue growth, the nuclei are a key component of the model. We chose to develop an off-lattice model where each nucleus is represented individually by a polygon. The choice of polygons is critical because it allows the deformation of nuclei, which is known to take place[S1]. Let N be the number of cells in the tissue. For each cell $i = 1, \dots, N$, its nucleus is represented by a polygon of N_p vertices. The position of the vertices is given by $X = (X_i^k)_{i \in [1,N], k \in [1,N_p]}$ with

$$X_i^k = (x_i^k, y_i^k) \quad \forall k \in [1; N_p], \forall i \in [1; N].$$

To simplify the notations in the following sections, we introduce some quantifiers that are specific to the nuclei. These quantifiers are not variables of the model and depend entirely on the polygon vertices X representing the nuclei. For each cell i=1,...,N, we denote as follows:

- $X_i = \frac{1}{N_p}\sum_{k=1}^{N_p} X_i^k$, the position of the center of mass of the nucleus i.
- $S_i = \sum_{k=1}^{N_p} \frac{1}{2}|X_iX_i^k \wedge X_iX_i^{k_+}|$, the surface of the nucleus i. The surface S_i of each nucleus i is computed by adding the area of every triangle $X_iX_i^kX_i^{k_+}$, with $k \in [1; N_p]$ and $k_+ \equiv k+1\ [N_p]$. The wedge symbol denotes the cross product between two vectors and [.] denotes the modulo operation (i.e. k [N] is the remainder in the Euclidean division of k by N). .
- $R_i = \sqrt{\frac{S_i}{\pi}}$, the radius such that the surface S_i of the nucleus i is equal to the surface of a ball with radius R_i.

The tissue is represented by an elastic box. We denote the edges of the box by $Y = (Y_j)_{j\in\{1,2,3,4\}} \in \mathbb{R}^2$ and consider the notations $j_\pm \equiv j \pm 1\ [4]$. The vertices of the box Y_j and Y_{j_+} are linked by springs of stiffness k_j^s and rest length l_j^s for $j \in [1,4]$. In addition, the angles of the box $(Y_{j_-}Y_jY_{j_+})$ are linked by torques of stiffness k_j^t and rest angle θ_j^t for $j \in [1,4]$. The springs and torques linking the vertices of the box allow deformation of the box to accommodate possible internal pressure created by the nuclei. Since the model aims to describe nuclear motion along the apical/basal (A-B) axis during the cell cycle, it is essential that the movements of the nuclei are restricted by vertical upper and lower bounds, representing the apical and basal surfaces.

Another major component of the model is the cable that mimics the effect of the cell membrane and associated cortex, which connects the basal to the apical surfaces. While these cables are not variables of the model, they are one of its essential ingredients. Indeed, their role of constricting the lateral movement of nuclei cannot be ignored when studying the motion of the nuclei during development. To avoid adding a lot of complexity to the model, the cell cortices are represented by an abstract straight line. For each cell i with $i = 1,\dots,N$, the coordinates of the attachment point of the cortex to the basal and apical surfaces are given by $M_i^b = (xm_i^b, ym_i^b) \in \mathbb{R}^2$ and $M_i^a = (xm_i^a, ym_i^a) \in \mathbb{R}^2$, respectively. The positions of the apical attachment point is fixed while the positions of the basal attachment can evolve over time to accommodate the surrounding forces.

Energies

Because the agents of the model rely on springs and torques, different energies arise from the system. These energies inform us on the way the elements of the model behave. We distinguish three categories for the energies of the model:

- The tissue energy $E_{tissue} = E_{box} + E_{ap}$ composed of the energy E_{box}related to the elasticity of the box and of the apical energy E_{ap}. The assembly of spring and torques linking the vertices of the box creates the energy of the box. It is given by

$$E_{box}(Y) = \sum_{j=1}^4 \frac{1}{2}k_j^s\left(\frac{|Y_j-Y_{j_+}|-\tau_j^s}{\tau_j^s}\right)^2 + \sum_{j=1}^4 \frac{1}{2}\frac{k_j^t}{\tau_j^{t2}}\left(\frac{Y_j-Y_{j_+}}{|Y_j-Y_{j_+}|}\cdot\frac{Y_j-Y_{j_-}}{|Y_j-Y_{j_-}|}-\tau_j^t\right)^2,$$

where $j_- \equiv j-1\ [4]$ for $j \in [1,4]$ and $(\tau_j^s)_{j\in[1,4]}$, $(\tau_j^t)_{j\in[1,4]}$ are the rest lengths and angles of the springs and torques respectively. The apical energy E_{ap} models a region

of length l^a near the apical surface where only dividing nuclei can enter. The expression of E_{ap} is calculated as follows:

$$E_{ap}(X,Y) = \sum_{i=1}^{N} \frac{1}{2} k_j^a \left(l^a - d_{(Y_1Y_2)}(X_i)\right)_+^2,$$

with the function $(u)_+ = \max(0,u)$ is the positive part function and $d_{(D)}(Z)$ is the distance of the point Z to the straight line (D).

- The nuclei energy E_{nuclei} models the cost of the deformation of the nuclei. In a resting position the nuclei are supposed to be in a spherical configuration. The nuclei energy E_{nuclei} is decomposed into two energies: the bending energy E_{bend}, acting on the angles of the polygon, and the perimeter energy E_{per}, acting on the lengths of the edges. These two energies are expressed by

$$E_{bend} = \sum_{i=1}^{N} \sum_{k=1}^{N_p} \frac{1}{2} k_1^b \left(\frac{\cos\left(\theta_i^k\right) - \cos\left(\theta_0^b\right)}{\cos\left(\theta_0^b\right)}\right)^2 + \sum_{i=1}^{N} \sum_{k=1}^{N_p} \frac{1}{2} k_1^b \left(\frac{\sin\left(\theta_i^k\right) - \sin\left(\theta_0^b\right)}{\sin\left(\theta_0^b\right)}\right)^2,$$

$$E_{per} = \sum_{i=1}^{N} \sum_{k=1}^{N_p} \frac{1}{2} k^p \left(\frac{|X_i^k X_i^{k_+}| - l_0^b}{l_0^b}\right)^2,$$

where θ_i^k is the angle $X_i^{k_-} X_i^k X_i^{k_+}$ and k_1^b, k_2^b, k^p are the stiffness of the energies and with $\theta_0^b = \frac{2\pi}{N_p}$ and $l_0^p = \frac{2\pi R_i}{N_p}$.

- The energy $E_{cable-to-nuclei}$ represents the action of the cable representing the cell cortex on the nuclei. In the tissue, for a given cell it is clear that the cell cortex constricts the lateral movement of the nucleus. In addition, we suppose that the cortex constraints the shape of nuclei. Then we consider that each vertex of a polygon X_i^k is linked by a spring of rest length zero to the cell cortex $(M_i^a M_i^b)$. The attachment of the spring on the cortex is defined such that the distance between the vertices and the cortex is minimal. The resulting energy created by the action of the cortex on the nuclei is defined as follows:

$$E_{cable-to-nuclei} = \sum_{i=1}^{N} \sum_{k=1}^{N_p} \frac{1}{2} k_i^c \left(\frac{|X_i^k P_{(M_i^a M_i^b)}(X_i^k)|}{R_i}\right)^2,$$

where $P_{(D)}(Z)$ is the projection of Z on the straight line (D) and k_i^c is the stiffness of the energy.

Constraints

To ensure the biological relevance of the model, some interactions between the different agents must be introduced. For example, it is crucial for the integrity of the tissue that the nuclei stay inside the elastic box. The interactions considered are various, including nuclei/nuclei interactions, nuclei/tissue interactions, nuclei/cable interactions, etc. These interactions are modeled by dimensionless inequality or equality constraints. To simplify the notations, the argument of the constraint functions are the polygon vertices X and the box vertices Y. We list the constraints considered in the model below.

- Nuclei/nuclei non-overlapping constraint φ^p : the constraint considered has the following form:

$$\varphi_{i_1,k,i_2}^p(X) \leq 0, \quad \forall (i_1,i_2) \in [1,N]^2, k \in [1,N_p],$$

where φ_{i_1,k,i_2}^p is defined later. Let us consider two cells i_1 and i_2 and one vertex k of the nucleus i_1. We denote by k^* the vertex of the polygon i_2 such that the quantity

$|d_{(X_{i_1}X_{i_2})}(X_{i_1}^k) - d_{(X_{i_1}X_{i_2})}(X_{i_2}^{k^*})|$ is minimal, with $d_{(D)}(Z)$ being the distance between the point Z and the straight line (D). Since there might be two solutions k_1^* and k_2^*, we choose k^* such that the distance between $X_{i_1}^k$ and $X_{i_2}^{k^*}$ is minimal. The expression of k^* is determined as follows:

$$k^* = \ argmin_{l\in[1,N_p],|X_{i_1}^k X_{i_2}^l|\leq|X_{i_1}X_{i_2}|}|d_{(X_{i_1}X_{i_2})}(X_{i_1}^k) - d_{(X_{i_1}X_{i_2})}(X_{i_2}^{\mathrm{l}})|.$$

Then the expression of the non-overlapping constraint is given by:

$$\varphi_{i_1,k,i_2}^p(X) = |X_{i_1}P_{(X_{i_1}X_{i_2})}(X_{i_1}^k)| + |X_{i_2}P_{(X_{i_1}X_{i_2})}(X_{i_2}^{k^*})| - |X_{i_1}X_{i_2}|.$$

- Nuclei/tissue non-overlapping constraint φ^t: to ensure the integrity of the tissue, it is necessary that the nuclei remain within the tissue. For this reason, we impose a non-overlapping constraint between the nuclei and the edges of the box. The non-overlapping between tissue and nuclei is expressed as follows:

$$\varphi_{i,k,j}^t(X,Y) \leq 0, \quad \forall i \in [1,N], k \in [1,N_p], j \in [1,4].$$

where $\varphi_{i,k,j}^t$ is defined by

$$\varphi_{i,k,j}^t(X,Y) = \frac{X_i^k X_i^{k-}}{|X_i^k X_i^{k-}|} \wedge \frac{Y_j X_i^k}{|Y_j X_i^k|}, \quad \forall i \in [1,N], k \in [1,N_p], j \in [1,4],$$

with $k_\pm \equiv \ k \pm 1 \ [N_p]$.

- Box constraints $\varphi^{b_1}, \varphi^{b_2}$: we choose to restrict the box movement by fixing the left bottom vertex of the box Y_4 to a given value $Y_0 = (x_0, y_0)$, and by fixing the vertical coordinate of the right bottom vertex of the box Y_3 to the value y_0. With this last constraint, the point Y_3 is able to slide on the horizontal axis given by $y = y_0$. The two constraints are calculated as follows:

$$\varphi_1^b(Y) = |Y_4 - Y_0| = 0 \quad \text{and} \quad \varphi_2^b(Y) = |y_3 - y_0| = 0.$$

- Surface constraint φ^s: while at a fixed time the nucleus can deform, its volume remains constant. Since the model is two-dimensional, the volume constraint translates into a surface constraint. Thus, we introduce a surface constraint intended to maintain the surface of a cell i to a surface S_i^0. The surface constraint is expressed as follows:

$$\varphi_i^s(X) = \frac{S_i - S_0^i}{S_0^i} = 0 \quad \forall i \in [1,N].$$

- Convexity constraint φ^c: the last constraint we impose on the system is the convexity of nuclei. The expression of the convexity constraint is calculated as follows:

$$\varphi_{i,k}^c(X) = \frac{X_i^k X_i^{k+}}{\left|X_i^k X_i^{k+}\right|} \cdot \frac{X_i^k X_i^{k-}}{\left|X_i^k X_i^{k-}\right|} \leq 0 \quad \forall i \in [1,N], k \in \left[1,N_p\right],$$

for $i \in [1,N]$, $k \in [1,N_p]$ and $k_\pm \equiv \ k \pm 1 \ \left[N_p\right]$.

Minimisation problem

At a given time of development, the system composed of the tissue and the nuclei is the solution of a minimisation problem. Therefore, the pseudostratified epithelium is described at all times by a minimal energy state. The variables of the minimisation problem are the polygon vertices X, representing the nuclei, the box vertices Y, representing the tissue, and the basal anchor points M^b. The potential W: $(\mathbb{R}^2)^{N\times N_p} \times (\mathbb{R}^2)^4 \times (\mathbb{R}^2)^N \longrightarrow \mathbb{R}$ created by the different energies of the system is defined by

$$W(X,Y,M^b) \ = \ E_{tissue}(Y) + E_{nuclei}(X) + E_{cable-to-nuclei}(X,Y,M^b).$$

The constraints applied to the system are the nuclei/nuclei non-overlapping constraints, nuclei/box non-overlapping constraints, box constraints, surface constraints, and convexity constraints. To simplify the notation, we consider that the inequality constraints and the equality constraints are expressed as follows:

$$\varphi^{v} \leq 0, \quad \forall v \in \{p, t, b_2, c\}, \quad \text{and} \quad \varphi^{v} = 0, \quad \forall v \in \{b_1, s\}.$$

We define by Q the set of admissible configurations of the system:

$$Q = \{(X, Y, M^b) \in (\mathbb{R}^2)^{N \times N_p} \times (\mathbb{R}^2)^4 \times (\mathbb{R}^2)^N | \varphi^p(X) \leq 0, \varphi^t(X, Y) \leq 0, \\ \varphi^{b_1}(Y) = 0, \varphi^{b_2}(Y) \leq 0, \varphi^s(X) = 0, \varphi^c(X) \leq 0\}.$$

The minimisation problem is formulated as follows: find $(\overline{X}, \overline{Y}, \overline{M^b}) \in (\mathbb{R}^2)^{N \times N_p} \times (\mathbb{R}^2)^4 \times (\mathbb{R}^2)^N$ such that

$$(\overline{X}, \overline{Y}, \overline{M^b},) = argmin_{(X,Y) \in Q} W(X, Y, M^b).$$

The potential W and the constraint functions φ^n, φ^t, φ^b, φ^s, φ^c are continuous but are not all necessarily convex. Therefore, the solution of the minimisation problem $(\overline{X}, \overline{Y})$may not be unique. We consider the Lagrangian $\mathcal{L}$: $(\overline{X}, \overline{Y}, \overline{M^b}) \in (\mathbb{R}^2)^{N \times N_p} \times (\mathbb{R}^2)^4 \times (\mathbb{R}^2)^N \to \mathbb{R}$ associated with the minimisation problem which is defined as follows:

$$\mathcal{L}(X, Y, M^b) = W(X, Y, M^b) + \lambda^p \varphi^p + \lambda^t \varphi^t + \lambda^{b_1} \varphi^{b_1} + \lambda^{b_2} \varphi^{b_2} + \lambda^s \varphi^s + \lambda^c \varphi^c,$$

where $\lambda^p = (\lambda^p_{i_1,k,i_2})_{(i_1,k,i_2) \in [i,N] \times [1,N_p] \times [1,N]}$, $\lambda^t = (\lambda^t_{i,k,j})_{(i,k,j) \in [i,N] \times [1,N_p] \times [1,4]}$, $\lambda^b = (\lambda^b_1, \lambda^b_2)$, $\lambda^s = (\lambda^s_i)_{i \in [1,N]}$, and $\lambda^c = (\lambda^s_{i,k})_{(i,k) \in [1,N] \times [1,N_p]}$ are the Lagrangian multipliers associated with the nuclei/nuclei non-overlapping constraints, nuclei/box non-overlapping constraints, box constraints, surface constraints, and convexity constraints, respectively. The notation $\lambda^v \varphi^v$ for $v \in \{p, t, b_1, b_2, s, c\}$ implicitly considers the element-by-element product. For example, for the surface constraint, $\lambda^s \varphi^s = \sum_{i=1}^{N} \lambda^s_i \, \varphi^s_i$.

Minimisation algorithm

The resolution of non-convex minimisation problems with constraints is not trivial. Because the system is not convex, a multitude of minima may exist. Note that our aim is not to find a global minimum of the problem but rather a local minimum. Indeed, in the system the actors seek to achieve the local optimum configuration closest to their initial configuration. The algorithm used to solve the minimisation problem is named the Damped Arrow-Hurwicz Algorithm (DAHA)[S2]. It is a modification of the classical Arrow-Hurwicz Algorithm with the addition of a damping term to ensure the convergence of the algorithm.

The DAHA algorithm is an iterative algorithm. The paramter τ denotes the index of the iteration. Knowing all previous iterates, the new iterate $\tau + 1$ is calculated as follows:

$$\begin{cases} {\lambda^p_{i_1,k,i_2}}^{\tau+1} = \max(0, {\lambda^p_{i_1,k,i_2}}^{\tau} + \beta^p \varphi^p_{i_1,k,i_2}(X^\tau)), \quad \forall (i_1, k, i_2) \in [1, N] \times [1, N_p] \times [1, N], \\ {\lambda^t_{i,k,j}}^{\tau+1} = \max(0, {\lambda^t_{i,k,j}}^{\tau} + \beta^t \varphi^t_{i,k,j}(X^\tau, Y^\tau)), \quad \forall (i, k, j) \in [1, N] \times [1, N_p] \times [1,4], \\ {\lambda^{b_1}}^{\tau+1} = {\lambda^{b_1}}^{\tau} + \beta^{b_1} |\varphi^{b_1}(Y^\tau)|, \\ {\lambda^{b_2}}^{\tau+1} = \max(0, {\lambda^{b_2}}^{\tau} + \beta^{b_2} \varphi^{b_2}(Y^\tau)), \\ {\lambda^s_i}^{\tau+1} = {\lambda^s_i}^{\tau} + \beta^s |\varphi^s_i(X^\tau)|, \quad \forall i \in [1, N], \\ {\lambda^c_{i,k}}^{\tau+1} = \max(0, {\lambda^c_{i,k}}^{\tau} + \beta^c \varphi^c_{i,k}(X^\tau)), \quad \forall i \in [1, N], k \in [1, N_p], \end{cases}$$

and

$$
\begin{cases}
Y_j^{\tau+1} = \dfrac{1}{1+{c_Y}/{2}}\left(2Y_j^{\tau} - \left(1-{c_Y}/{2}\right)Y_j^{\tau-1}\right) - \dfrac{\alpha_Y^2}{1+{c_Y}/{2}}\nabla_{Y_j}\mathcal{L}\left(X^{\tau}, Y^{\tau}, M_k^{b\,\tau}\right) \\
\quad - \dfrac{\gamma^{Y,t}}{1+{c_Y}/{2}} \sum_{\substack{(i,k)\in[1,N]\times[1,N_p] \\ j\in[1,4]}} \varphi_{i,k,j}^{t}(X^{\tau}, Y^{\tau})\lambda_{i,k,j}^{t}\nabla_{Y_j}\varphi_{i,k,j}^{t}(X^{\tau}, Y^{\tau}) \\
\quad - \dfrac{\gamma^{Y,b_1}}{1+{c_Y}/{2}}\varphi^{b_1}(Y^{\tau})\lambda^{b_1}\nabla_{Y_j}\varphi^{b_1}(Y^{\tau}) \\
\quad - \dfrac{\gamma^{Y,b_2}}{1+{c_Y}/{2}}\varphi^{b_2}(Y^{\tau})\lambda^{b_2}\nabla_{Y_j}\varphi^{b_2}(Y^{\tau}), \forall\ \mathrm{j} \in [1,4], \\
M_k^{b\,\tau+1} = \dfrac{1}{1+{c_M}/{2}}\left(2M_k^{b\,\tau} - \left(1-{c_Y}/{2}\right)M_k^{b\,\tau-1}\right) - \dfrac{\alpha_M^2}{1+{c_M}/{2}}\nabla_{M_k^b}\mathcal{L}\left(X^{\tau}, Y^{\tau}, M_k^{b\,\tau}\right) \\
X_k^{i\,\tau+1} = \dfrac{1}{1+{c_X}/{2}}\left(2X_k^{i\,\tau} - \left(1-{c_X}/{2}\right)X_k^{i\,\tau-1}\right) - \dfrac{\alpha_X^2}{1+{c_Y}/{2}}\nabla_{X_k^i}\mathcal{L}\left(X^{\tau}, Y^{\tau}, M_k^{b\,\tau}\right) \\
\quad - \dfrac{\gamma^{X,p}}{1+{c_X}/{2}} \sum_{\substack{(i_1,i_2)\in[1,N]^2 \\ k\in[1,N_p]}} \varphi_{i_1,k,i_2}^{p}(X^{\tau})\lambda_{i_1,k,i_2}^{p}\nabla_{X_k^i}\varphi_{i_1,k,i_2}^{p}(X^{\tau}) \\
\quad - \dfrac{\gamma^{X,t}}{1+{c_X}/{2}} \sum_{\substack{(i,k)\in[1,N]\times[1,N_p] \\ j\in[1,4]}} \varphi_{i,k,j}^{t}(X^{\tau}, Y^{\tau})\lambda_{i,k,j}^{t}\nabla_{X_k^i}\varphi_{i,k,j}^{t}(X^{\tau}, Y^{\tau}) \\
\quad - \dfrac{\gamma^{X,s}}{1+{c_X}/{2}} \sum_{i\in[1,N]} \varphi_i^{s}(X^{\tau})\lambda_i^{s}\nabla_{X_k^i}\varphi_i^{s}(X^{\tau}) \\
\quad - \dfrac{\gamma^{X,c}}{1+{c_X}/{2}} \sum_{(i,k)\in[1,N]\times[1,N_p]} \varphi_{i,k}^{c}(X^{\tau})\lambda_{i,k}^{c}\nabla_{X_k^i}\varphi_{i,k}^{c}(X^{\tau}), \forall\ \mathrm{i} \in [1,\mathrm{N}], \mathrm{j} \in \left[1, N_p\right],
\end{cases}
$$

where α_Y, α_X, α_M are parameters that control the actualisation of the variables X, Y and M^b, β^p, β^t, $\beta^b = (\beta^{b_1}, \beta^{b_2})$, β^s and β^c are parameters that control the actualisation of the Lagrangian multipliers and $\gamma^{Y,t}$, γ^{Y,b_1}, γ^{Y,b_2}, $\gamma^{X,p}$, $\gamma^{X,t}$, $\gamma^{X,c}$, $\gamma^{X,s}$, c_Y, c_X and c_M are actualisation parameters.

The stopping criterion of the minimisation algorithm is determined by

$$\frac{\mathcal{L}(X^{\tau+1}, Y^{\tau+1}) - \mathcal{L}(X^{\tau}, Y^{\tau})}{\mathcal{L}(X^{\tau}, Y^{\tau})} \leq \epsilon,$$

where $\epsilon > 0$ is the tolerance. This condition ensured that the Lagrangian variations were small and therefore that the minimum configuration of the system is close enough, depending on the threshold ϵ. We fix $\epsilon = 10^{-5}$.

The parameters α are related to the speed of actualisation of the position of the polygons and the box vertices in the opposite direction of the gradient of the Lagrangian (and therefore of the potential W). The speeds of actualisation of the Lagrangian multipliers associated with the constraints are controlled by the parameters β. The parameters γ control the weight of the constraints in the Lagrangian. In the initial version of the DAHA[S2], the parameters γ are

calculated using $\gamma = \alpha\beta$. However, it has been observed by the authors that considering γ independent of α and β leads to faster convergence results. It explains why γ are full-fledged parameters in this model. The parameters c are related to the damping term. In accordance with [2] we fixed $c_X = c_Y = c_{M^b} = 2$ because it has been observed that it provides better results. The values of α, β, and γ listed below have been chosen to ensure a rapid convergence of the system to the minimal energy state.

	X	Y	M^b
α	0.1	0.1	0.1
c	2	2	2

	φ^p	φ^t	φ^{b_1}	φ^{b_2}	φ^s	φ^c
β	0.1	0.1	1	1	0.01	0.1
γ	0.01	0.5	1	1	1	0.01

Time-dependent model: the cell cycle

We introduce the time dependency part of the model. During the development of the tissue, cells are subject to the cell cycle, which describes the process that cells undergo to divide. It is composed of four phases: G_1, S, G_2, and M. Let us consider the time $t \in [0, T]$ with $T > 0$. We introduced a time discretization $(t^n)_{n\in[0,N_t]}$ of $[0, T]$ with $t^n = t^{n-1} + dt$ where $dt > 0$. At each time step t^n, a cell i is in a phase of the cell cycle, namely G_1, S, G_2, or M. In the model the M phase is divided into 3 steps, while the other phases are described by one step each. Accordingly, the total number of steps in the model is 6 6 (see Figure 2D). The various steps are described in the following paragraphs.

- Steps 0 (equivalent to G_1): the phase 0 is characterised by an apical-to-basal movement of the nuclei along their cortex. In the fish retina[S3] and mouse brain[S4] this motion is considered passive. It is a consequence of other cells going through the cell cycle pushing neighbouring cells away to reach the apical surface, sending new daughter cells inside the depth of the tissue. In the model, this phase was therefore characterized by passive motion.
- Steps 1 (equivalent to S): for simplicity we decided to limit the growth of the nucleus to this phase. When a cell enters this phase at time t^{n^*}, a clock $C_i^{n_*}$ is defined to determine the time the nucleus remains in S. In the model, the increase of the volume is given by an increase in surface area. Let us consider a nucleus i that enters phase 1 at time $t_* = t^{n_*}$. The number of iterations in which the nucleus has to double its volume is given by $\overline{n}_i = \frac{\lfloor c_i^{n_*} \rfloor}{dt}$. The increase of surface area is then calculated as follows:
$$S_i^n = \pi(R_i^{n_*3} + \frac{n-n^*}{\overline{n}_i} R_i^{n_*3})^{2/3}.$$
- Steps 2 (equivalent to G_2): phase nuclei migrate towards the apical region. We suppose that this motion is active[S3-S5]. The implementation of the active movement is made via the addition of an energy E_{IKNM} during the minimisation. At the cell level, apical movement is executed by the action of actomyosin[S6,S7]. We chose to model this action with a spring linking the centre of mass of the nucleus to the apical point of its

cortex. During G_2, the rest length of the spring is fixed to zero. Such a configuration induces the drag of the nuclei towards the apical region. Therefore, the energy E_{IKNM} is calculated as follows:

$$E_{IKNM}(X) = \sum_{i\in[1,N_p],P_i=2} \frac{1}{\zeta} k^{IKNM} \left(\frac{|X_i - M_i^a|}{\tau_2^s}\right)^{\zeta},$$

where k^{IKNM} is the stiffness of the spring and zeta is a parameter linked to the type of spring. Fixing $\zeta = 1$ induces the force to be constant while $\zeta = 2$ describes a hookean spring. To simulate the fact that the upward movement is not continuous in vivo[S3-S5], we define the apical-ward motion as a processive mechanism whereby the underlying motor can engage and disengage. In the model, we considered that this mechanism takes some time to organise and can also break. Let p_{IKNM}^{on} and p_{IKNM}^{off} denote the probability of engaging and disengaging the motor driving apical-ward movement, respectively. The deacrease of p_{IKNM}^{on} and the increase of p_{IKNM}^{off} then slow down the active motion in G_2. The creation of the new energy in the minimisation causes the introduction of another energy into the system. So far, all the movements associated with the minimisation are internal and independent of time. However, the apical-ward movement energy produces a time-dependent process that takes place over many time iterations. In the absence of other constraints, a lone nucleus would be able to cross the whole depth of the tissue in one iteration. To prevent this, we introduced a gradient flow energy. This energy adds a weight to the movement of the nucleus. At each time step t^n, the energy E_{GF} is expressed as follows:

$$E_{GF}(X) = \sum_{i\in[1,N_p]} \frac{1}{2} k^{GF} \left(\frac{|X_i - X_i^n|}{X_i^n}\right)^2,$$

with k^{GF} as the stiffness of the energy.

Once the nucleus i is close enough to the apical surface, i.e. $\left|d_{(Y_1Y_2)}(X_i) - \epsilon^{G_2}\right| \leq 0$ with $\epsilon^{G_2} > 0$ as a small threshold, the nucleus enters mitosis. Mitosis is the fastest phase of the cell cycle. However, in the model we split this phase in three steps, are described as follows:

1. Steps 3: Nuclei undergo mitosis in a narrow apical zone where only dividing nuclei can enter[S6]. There, nuclei round up, pushing neighbors away[S8,S9] . During this phase the apical stiffness energy k_i^a is set to zero. In this region, nuclei are located above all the other nuclei and, being free of pressure, become spherical. In this subphase, we set the stiffness of the cable energy to zero $k_i^c = 0$.
2. Steps 4 of the model corresponds to actual mitosis. Since this process is fast compared to the duration of the cell cycle, we considered this step to happen in one iteration. Let us consider a nucleus i in phase 4 at time t^n and its two daughter nuclei of indices i_1 and i_2. The new daughters are characterised by the surface $S_{i_1}^{n+1}$ and $S_{i_2}^{n+1}$, both of which are equal to half the surface of the mother nucleus S_i^n. It is known that nuclei divide perpendicular to the apical plane. To satisfy this condition, the position of the daughter cell is computed with the following steps:
   Let N^* be the floor value of $\frac{N_p}{2}$. Find the indices l_0 such that $[X_i^l, X_i^{l+N^*}]$ is as perpendicular as possible to the apical surface $[Y_1, Y_2]$, i.e.,

$$l_0 = argmin_{l\in[1,N^*]} X_i^l X_i^{l+N^*} \cdot Y_0 Y_1$$

   a. Define the position of the first N^* vertices of the polygons representing the two daughter nuclei:

$$X_{i_1}^l = X_i^{l_0-1+l} \quad \text{and} \quad X_{i_2}^l = X_i^{l_0+N^*-1+l}, \quad \forall l \in [1, N^*].$$

b. Complete the definition of the last N^* vertices of the polygons representing the two daughter nuclei:

$$X_{i_1}^l = X_i^{l_0+N^*-1} + \left(\frac{l-N^*}{N^*+2}\right) * (X_i^{l_0} - X_i^{l_0+N^*}), \quad \forall l \in [N^*, N_p]$$

and

$$X_{i_2}^l = X_i^{l_0-1} + \left(\frac{l-N^*}{N^*+2}\right) * \left(X_i^{l_0+N^*} - X_i^{l_0-1}\right), \quad \forall l \in [N^*, N_p].$$

The different steps of the definition of the daughter nuclei are represented in Fig. A2. Note that to store the value of the new cells, one of the daughter nuclei is stored in the place of its mother, while the other one is created as a new nucleus.

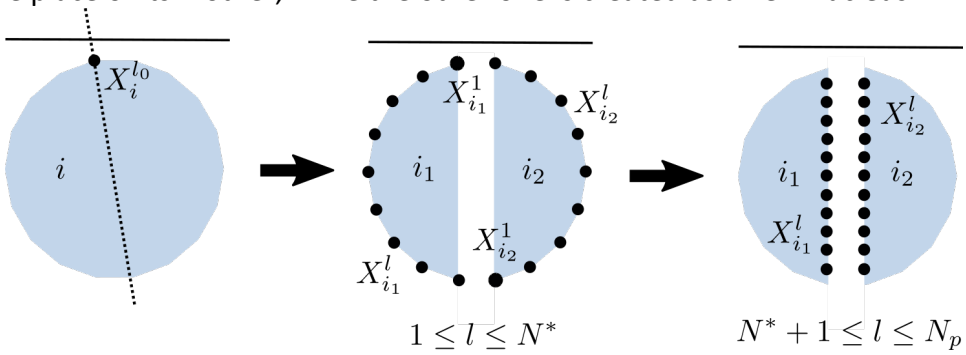

Fig. A2: Representation of the different steps leading to the division of a nucleus i. Left: Step a; Middle: Step b; Right: Step c.

3. Steps 5: The last phase of the model is related to construction of the cable (cell cortex) of the two new daughter nuclei. One of the daughter nuclei will keep the cable of its mother[S10]. This nucleus then enters phase 0. The other nucleus i_2 will enter phase 5 to be given time to construct its cortex. The average time T_3 spent by the nucleus in this phase is considered to be equal to 12 minutes. The creation of the cortex associated with nucleus i_2 is made to ensure that the cables are ordered and do not cross. The new cortex anchor points $M_{i_1}^a$ and $M_{i_1}^b$ are chosen randomly in the intervals

$$I^a = \left[P_{(Y_1Y_2)}(X_{i_2}) - v, P_{(Y_1Y_2)}(X_{i_2}) + v\right] \cap \left[M_{j_-}^a, M_{j_+}^a\right],$$

and

$$I^b = \left[P_{(Y_3Y_4)}(X_{i_2}) - v, P_{(Y_3Y_4)}(X_{i_2}) + v\right] \cap \left[M_{j_-}^b, M_{j_+}^b\right],$$

respectively, with j_- and j_+ as the indices defining the nuclei directly to the left and right of the nucleus i_2. The parameter v is given by $v = 2^k R_{i_2}$, with k as the smallest integer such that the sets I^a and I^b are not empty.

This concludes the description of the cell cycle phases. The duration of theses phases are denoted by $T_0, T_1, T_2, T_3, T_4, T_5$ respectively. In addition, we consider the growth of the elastic box. For the sake of simplicity, the vertical dimension of the box (along the apical-basal axis) is fixed and set to provide sufficient space for multiple layers to form. This assumes that the basal surface does not constrain growth (as suggested by Fig.1B) although we cannot exclude the possibility that actin accumulation could impair the free mouvement of nuclei in this region[S1]. In contrast, we expect the lateral sides of the box to constrain growth. This is represented by allowing elastic deformation of the box perpendicular to the apical-basal axis. To allow progressive expansion of the box, at a given time step t^n, the lateral rest length of

the spring of the elastic box is updated $\tau_J^{s^{n+1}} = |\overline{Y_J^{n+1}} - \overline{Y_{J_+}^{n+1}}|$ with $\bar{Y}$ the solution of the minimisation problem and J the indices corresponding to the lateral spring.

Choice of the model parameters

To finish the presentation of the model we discuss the choice of its parameters. The aim of this project is to reproduce the development of the imaginal disc of Drosophila. Therefore, whenever possible, parameter values are chosen in accordance with experimental results. However, in some situations, it was difficult to relate parameters to actual data, therefore, some approximations had to be made.
To initialise the model we considered data given from [S11]. This shows that at $t = 36h$, around 70% of the cells are in the S phase, 30% in G_1, and 0% in G_2. In the model we decided to start with a small number of nuclei $N = 10$ at a developmental time of $60h$. We initialised the model with seven nuclei in the S phase and three nuclei in G_1. The initialisation of the positions of the nuclei and the elastic box are made to match the configuration of the imaginal disc of Drosophila. We initialised the nuclei and box as follows:

- The tissue was initialised as a rectangular box. The vertices of the box are defined as follows: $Y_1 = (-5, 4)$, $Y_2 = (5, 4)$, $Y_3 = (5, -4)$, and $Y_4 = (-5, -4)$.
- The nuclei were initialised on the horizontal line of coordinate $y = 0.5$ such that the nuclei were spread uniformly on this axis. This position was then perturbed by a small noise. For all $i \in N^{ini}$, the position of the vertices of the polygons are given as follows:
  $X_i^l = X_i + R_i \begin{pmatrix} \cos(\frac{2l\pi}{N_p}) \\ \sin(\frac{2l\pi}{N_p}) \end{pmatrix} \forall l \in [1, N_p]$, with $X_i = (-4.5 + i - 1.,0.5) + 0.5R_i\epsilon_X$
  with X_i as the position of the center of mass of the polygon and ϵ_X as a random number between zero and one chosen according to a uniform law. The radius R_i depends of the cell cycle phase the nuclei i is into. If the nuclei i is in phase G_1, then $R_i = 0.5$. For the rest of the annexwe call this value $R^{ini} = 0.5$. If the nuclei i is in phase S, R_i is chosen randomly between R^{ini} and $2^{2/3}R^{ini}$. It models the distribution of the nuclei in phase S. The number of vertices of the polygon is fixed to $N_p = 20$. This parameter is chosen to be large enough to observe the deformation and the motion of the nuclei but small enough to avoid large computational times.

In order to be able to observe phenomena with a duration of less than an hour we choose as a time step $dt = \frac{1}{10}h = 6\ min$. In addition to the information on the distribution of the nuclei in G_1, S, and G_2 during development of the imaginal disc of Drosophila, the reference [S11] also gives us information about the duration of the cell cycle phases as a function of the development time.

As previously mentioned, T_0, T_1, T_2, T_3, T_4 and T_5 are the average durations of the different steps of the model. Notice that these durations can depend on time. The choice of these durations (except for T_2, which is an output of the model) has been made with information presented in [S11] as outlined next:

- We observed that the average duration of G_1 increases over time. With a basic regression, we choose $T_0(t) = (\frac{t}{24})^2$ with t as the time in hours.

- The duration of the S phase seems to be roughly constant. We choose $T_1(t) = 8h$.
- The disengagement of the cortex action on a nucleus that has reached the apical surface is considered to happen over a short period of time (within a few minutes). Therefore, we have $T_3(t) = dt + 2\epsilon_3 dt$ with ϵ_3 as a random number between zero and one chosen according to a uniform law.
- The division of the nuclei is assumed to be instantaneous. Therefore, $T_4(t) = 0$.
- The construction of the new cortex is considered to take a few minutes, meaning that $T_5(t) = dt + 2\epsilon_5 dt$ with ϵ_5 as a random number between zero and one chosen according to a uniform law.
-

The other parameters that need to be defined are p_{IKNM}^{on} and p_{IKNM}^{off}. These two parameters provide the probability of engagement of a given nucleus with the machinery that drags it towards the apical surface. We consider that these mechanisms follow Poisson processes of parameters ν^{on} and ν^{off}, respectively. This means that the probability of starting and stopping the mechanism during a time interval dt can be approximated by

$$p_{IKNM}^{on} = 1 - e^{\nu^{on} dt} \quad and \quad p_{IKNM}^{off} = 1 - e^{\nu^{off} dt},$$

provided that dt is so small that $\nu^{on} dt \ll 1$ and $\nu^{off} dt \ll 1$. We assumed that motor engagement occurs frequently, 10 times an hour. Therefore, $\nu^{on} = 10\, h^{-1}$. To ensure that the global movement of the nuclei was oriented towards the apical membrane, we determined that the probability to disengage must be smaller than the probability to engage the motor. However, if nuclei were prevented from moving because of other nuclei, we supposed that the probability to disengage would become larger. We defined t^{IKNM} as the time in which the nuclei position has moved by a distance smaller than $0.5R^{ini}$. We then choose

$$\nu^{off} = \overline{\nu}^{off}(1 + \frac{t^{IKNM}}{t_0^{IKNM}}),$$

with $\overline{\nu}^{off} = 1\, h^{-1}$ as the frequency of the event when the nucleus is moving and t_0^{IKNM} as the time it takes for a nucleus to reach the apical membrane without any exterior constraint. This time is expected to be between 30 minutes and 1 hour. In this case, we choose $t_0^{IKNM} = 1$ h.

The last parameters to define are the ones related to the energies. They are defined as follow:

- We first considered the energies related to the elastic box. We considered the springs and torques of the box to be of the same order as those related to the nuclei and cell cortex. We then chose $k^s = 1$ and $k^t = 1$. The rest length and rest angles were chosen such that the equilibrium position is that at initialisation. This means that $l_1^s = l_3^s = 10$, $l_2^s = l_4^s = 8$ and $\tau_j^t = \pi/2$ for $j \in \{1,4\}$.
- The apical energy prevents nuclei from getting too close to the apical membrane. So that this energy is stronger than the one of the nuclei, we choose $k_i^a = 10\ if\ C_i \in \{0,1\}$ and $k_i^a = 0$ if $C_i \in \{2,3,4,5\}$. The thickness of the apical layer was chosen to be $l^a = 3R^{ini}$.
- The distance energy models the action of the cell cortex on nuclei while the bending energy models the preferred shape of the nuclei. Here we have chosen parameters that reproduce experimental nuclear shapes. On this basis, we have fixed $k_1^b = 0.1$ and $k^c = 0.1$.
- The IKNM energy controls the migration of the nuclei in the G_2 phase (equivalent to phase 2 in the model); therefore, for a given nucleus i, when $C_i \in \{0,1,3,4,5\}$,

$k_i^{IKNM} = 0$. When $C_i = 2$, we consider $k_i^{IKNM} = k^{IKNM}$, which does not depend on time. Given that at early stages the duration of G_2 is less than one hour, we fix $k^{IKNM} = 0.05$ and $k^{GF} = 0.01$ so that the duration for one nucleus to reach the apical membrane is between 30 minutes and 1 hour.

In the paper, each model simulation has been run for 20 initialisations. The difference between each initialisation is produced by a change of the random seed (all the other parameters are similar). For an initialisation ini the seed is defined by the following FORTRAN code:

```
call Random_seed(size = n)
allocate(seed(n))
seed = ini + 37 * (/ (i - 1, i = 1, n) /)
call Random_seed(PUT = seed)
deallocate(seed)
```

Analysis of the simulations

In this section we describe the tools used to analyse the results of the Individual-Based Model. In particular we detail the quantifiers used in this study: the number of layer, the crowding, the apical/basal position of the nuclei, the average time spent in G_2, velocity of the nuclei during the last hour in G_2. The numerical simulations have been performed in FORTRAN and we compare the results of 20 initialisations.
In the simulations, we observe an increase in the number of layers of nuclei. To quantify this increase in the numerical simulations we study the quantity

$$N_l = \frac{2RN}{(|Y_1 - Y_2| + |Y_3 - Y_4|)/2},$$

as a function of the time iteration (see Fig. 5F). As previously mentioned, N is the number of nuclei at a given time and R is the radius of a spherical nuclei in the G_1 phase. The distance $(|Y_1 - Y_2| + |Y_3 - Y_4|)/2$ represents the average length of the box, taking into account its possible deformation. The formula $\frac{|Y_1 - Y_2| + |Y_3 - Y_4|)/2}{2R}$ then corresponds to the number of nuclei organised in one layer that can fit in the length of the tissue. Therefore, N_l gives us an insight into the number of layers of nuclei present in the tissue at a given time.

The apical basal depth of the nuclei in the tissue is quantified by considering the average depth of the nuclei in the tissue $D = \frac{1}{N} \sum_{i=1}^{N} d_{(Y_1 Y_2)}(X_i)$. This quantity is presented in Fig. 3B.

Another parameter we are interested in is the crowding observed in the tissue. To quantify this increase in the simulation, we computed the crowding in a similar manner to the experimental data treatment presented in Fig. 1F with the difference that surfaces are considered instead of volumes. This quantity is plotted in Figs. 3C and 5F).

To compare the overall behaviours of the nuclei as functions of space we consider the distribution of the nuclei in phases G_1, S, and G_2 along the A-B axis (see Figs. 3G and 5B). In the simulations, the apical/basal axis was discretised in small subsets of length $h = 0.2R^{ini}$. For each subset, the number of nuclei in G_1, S, and G_2 were computed. We then had the

number of nuclei in each of the phases relative to the position on the basal/apical axis. This value can be reformulated to obtain the number of nuclei in each of the phases as a function of the apical distance.

Finally we are interesting in the evolution of the nuclei during G_2. Let $it_{G_2}^{in}(i)$ and $it_{G_2}^{out}(i)$ be the iteration number corresponding to the time a nucleus i enters and leaves G_2, respectively. Then we can compute the average time $T_{G_2}^{in/out}$ needed for a nucleus that has entered G_2 to reach the apical membrane. $T_{G_2}^{in/out}(t)$ is then calculated as follows:

$$T_{G_2}^{in/out}(t) = \frac{dt}{Card(\overline{Q}_{G_2}^{it})} \sum_{i \in \overline{Q}_{G_2}^{it}} |it_{G_2}^{out}(i) - it_{G_2}^{in}(i)|,$$

with $\overline{Q}_{G_2}^{it} = \{i \in [1, N] | it_{G_2}^{in}(i) \leq it \leq it_{G_2}^{out}(i)\}$. In addition we compute the apical distance $D_{G_2}^{in/out}$ of the nuclei to the apical membrane when they enter the phase G_2:

$$D_{G_2}^{in/out}(t) = \frac{dt}{Card(\overline{Q}_{G_2}^{it})} \sum_{i \in \overline{Q}_{G_2}^{it}} |X_i^{it_{G_2}^{out}(i)} - X_i^{it_{G_2}^{in}(i)}|.$$

Finally, we consider the velocity $V_{G_2}^{out_{1h}}$ of the nuclei in the hour before their division:

$$V_{G_2}^{out_{1h}}(t) = \frac{dt}{Card(\tilde{Q}_{G_2}^{it})} \sum_{i \in \overline{Q}_{G_2}^{it}} \frac{|X_i^{it_{G_2}^{out}(i)} - X_i^{it_{G_2}^{out}(i)-1}|}{1},$$

with $\tilde{Q}_{G_2}^{it} = \{i \in [1, N] | it_{G_2}^{out}(i) - 1 \leq it \leq it_{G_2}^{out}(i)\}$.

Description of the basal mechanism

We hypothesise that the nuclei are able to transition from G_1 to S when the nuclei receive a signal from the basal membrane. We define the range of diffusion by λ.

In the model, the transition to the S phase is considered to follow a Poisson process of parameters $\nu_{G_1/S}$. This means that the probability $P_{G_1/S}$ of a nucleus in G_1 changing phase at each time step is approximated by

$$P_{G_1/S} = 1 - e^{-\nu_{G_1/S} dt},$$

provided that dt is small enough to verify $\nu_{G_1/S} dt \ll 1$. The parameter $\nu_{G_1/S}$ is idealistically computed as a function of the distance of a nucleus to the basal membrane. However, in the model, the width of the box is fixed, which is not the case in real tissue. Therefore, the probability $P_{G_1/S}$ is instead a function of the distance of a given nucleus to the nucleus that is the closest to the basal membrane at the time of its birth. At a given birth time , we denote by i_t^* the nucleus that is the closest to the basal membrane. Then the distance to the basal membrane is given by $d_b = d_{(Y_3 Y_4)}(X_j) - d_{(Y_3 Y_4)}(X_{i_t^*})$. We define the probability of a nucleus j to transition from G_1 to S of at time t as follows:

$$\nu_{\frac{G_1}{S}}(j, t) = 30 \overline{\nu}_{G_1/S} e^{-\frac{\ln(0.1)}{\lambda} d_b} 1_{d_b \leq \lambda},$$

with $\overline{\nu}_{G_1/S}$ and λ the maximal frequency and the diffusion length, respectively. This formula means that the frequency of the transition from G_1 to S for the nuclei that are closest to the basal membrane is $\overline{\nu}_{G_1/S}$. The frequency decreases to zero for nuclei located at a distance λ from the nucleus i_t^*, meaning that the probability of entering S is equal to zero. The probability is then set to zero for the rest of the nuclei. The frequency $\overline{\nu}_{G_1/S}$ is set to 0.7 per hour, meaning that the transition of the nuclei closest to the basal membrane occurs less than

once every hour. The diffusion length varies between 2, 4 and 10 depending on the simulations.

ADDITIONAL REFERENCES

S1. Lele, T.P., Dickinson, R.B., and Gundersen, G.G. (2018). Mechanical principles of nuclear shaping and positioning. J Cell Biol *217*, 3330-3342. 10.1083/jcb.201804052.

S2. P. Degond, M.A.F., and S. Motsch (2017). Damped arrow–hurwicz algorithm for sphere packing. Journal of Computational Physics, 332:347

S3. Leung, L., Klopper, A.V., Grill, S.W., Harris, W.A., and Norden, C. (2011). Apical migration of nuclei during G2 is a prerequisite for all nuclear motion in zebrafish neuroepithelia. Development *138*, 5003-5013. 10.1242/dev.071522.

S4. Okamoto, M., Shinoda, T., Kawaue, T., Nagasaka, A., and Miyata, T. (2014). Ferret-mouse differences in interkinetic nuclear migration and cellular densification in the neocortical ventricular zone. Neurosci Res *86*, 88-95. 10.1016/j.neures.2014.03.011.

S5. Norden, C., Young, S., Link, B.A., and Harris, W.A. (2009). Actomyosin is the main driver of interkinetic nuclear migration in the retina. Cell *138*, 1195-1208. 10.1016/j.cell.2009.06.032.

S6. Meyer, E.J., Ikmi, A., and Gibson, M.C. (2011). Interkinetic nuclear migration is a broadly conserved feature of cell division in pseudostratified epithelia. Curr Biol *21*, 485-491. 10.1016/j.cub.2011.02.002.

S7. Liang, L., Haug, J.S., Seidel, C.W., and Gibson, M.C. (2014). Functional genomic analysis of the periodic transcriptome in the developing Drosophila wing. Dev Cell *29*, 112-127. 10.1016/j.devcel.2014.02.018.

S8. Stewart, M.P., Helenius, J., Toyoda, Y., Ramanathan, S.P., Muller, D.J., and Hyman, A.A. (2011). Hydrostatic pressure and the actomyosin cortex drive mitotic cell rounding. Nature *469*, 226-230. 10.1038/nature09642.

S9. Matthews, H.K., Delabre, U., Rohn, J.L., Guck, J., Kunda, P., and Baum, B. (2012). Changes in Ect2 localization couple actomyosin-dependent cell shape changes to mitotic progression. Dev Cell *23*, 371-383. 10.1016/j.devcel.2012.06.003.

S10. Kosodo, Y., and Huttner, W.B. (2009). Basal process and cell divisions of neural progenitors in the developing brain. Dev Growth Differ *51*, 251-261. 10.1111/j.1440-169X.2009.01101.x.

S11. Wartlick, O., Mumcu, P., Kicheva, A., Bittig, T., Seum, C., Julicher, F., and Gonzalez-Gaitan, M. (2011). Dynamics of Dpp signaling and proliferation control. Science *331*, 1154-1159. 10.1126/science.1200037.

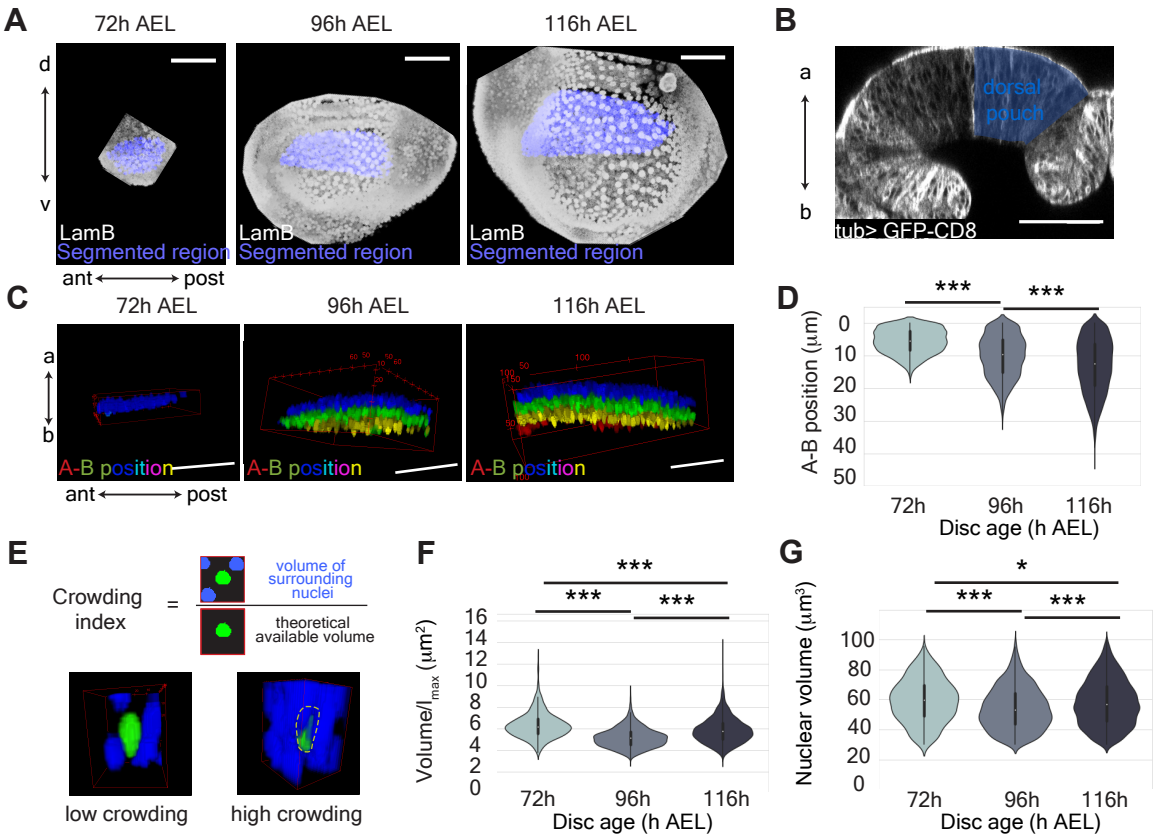
A
72h AEL
96h AEL
116h AEL
d
v
LamB
Segmented region
ant
post
B
a
b
dorsal pouch
tub> GFP-CD8
C
A-B position
D
***
A-B position (µm)
Disc age (h AEL)
E
Crowding index
=
volume of surrounding nuclei
theoretical available volume
low crowding
high crowding
F
Volume/I$_{max}$ (µm^2)
G
*
Nuclear volume (µm^3)

Figure S1: Nuclear organisation in a growing wing imaginal disc of Drosophila. Related to Figure 1. (A) Max projection of 72h, 96h and 116h AEL wing imaginal discs stained with anti-Lamin B (white) and mounted in an agar drop infused with FocusClear^{TM}. The Nessys Module of the PickCells program, and custom algorithms (see Methods) were used to identify nuclei. Our analysis was confined to the pouch, the area that gives rise to the wing proper. And to ease segmentation, which still requires manual correction, only the dorsal compartment was considered since its behaviour can be considered representative of the whole pouch ([S1,S2]). Nuclei located near the dorso-ventral boundary were not included in the analysis since they terminate proliferation in response to a specific genetic program [S3]. Thus, in the blue-shaded areas, we catalogued 836 nuclei from 4 discs at 72h after egg laying (AEL), 2562 nuclei from 4 discs at 96h AEL and 5889 nuclei from 3 wing discs at 120h AEL. **(B)** Optical cross-section of a 116h AEL wing imaginal disc expressing CD8-GFP to highlight cell membranes. The region where nuclei were segmented (the dorsal compartment) is shaded blue. (**C)** 3D reconstruction of segmented nuclei from the discs showed in A and C. Nuclei are colour-coded according to their depth along the apical-basal axis. Note the increased number of layers. (**D)** Distribution of nuclei along the apical-basal (in μm) axis in 72h, 96h and 116h AEL wing discs. As discs grow, nuclei are increasingly occupying more basal positions (72h AEL: 4 discs, 836 nuclei. 96h AEL: 4 discs, 2562 nuclei. 116h AEL: 3 discs: 5889 nuclei). (**E)** Crowding index and examples of a low and high crowding situation. A crowding index was measured for each nucleus by first creating a box enclosing the nucleus of interest 30 pixels beyond the edge of the nuclei in the x and y axis, and 10 pixels in the z axis. We then measured the proportion of voxel occupied by other nuclei (volume of surrounding nuclei) in this box (theoretical available volume). **(F-G)** Nuclear 'roundness' (V/I^{max}) along the A-B axis and the distribution of nuclear volumes (μm^3) at three developmental times. The biphasic trend for both parameters (down between 72 and 96 hAEL and up between 96 and 116 hAEL) is consistent with the observations of Kirkland and colleagues [S4]. This is not predicted by the model; it could result from additional physiological or mechanical features not incorporated in our model [S5-S7]. Data was from 72h AEL: 4 discs, 836 nuclei. 96h AEL: 4 discs, 2562 nuclei. 116h AEL: 3 discs: 5889 nuclei. Wilcoxon rank-sum statistic test for two samples was performed in B-D. * $P<0.5$ *** $P<0.001$. The scale bars in the figure represents 50 μm.

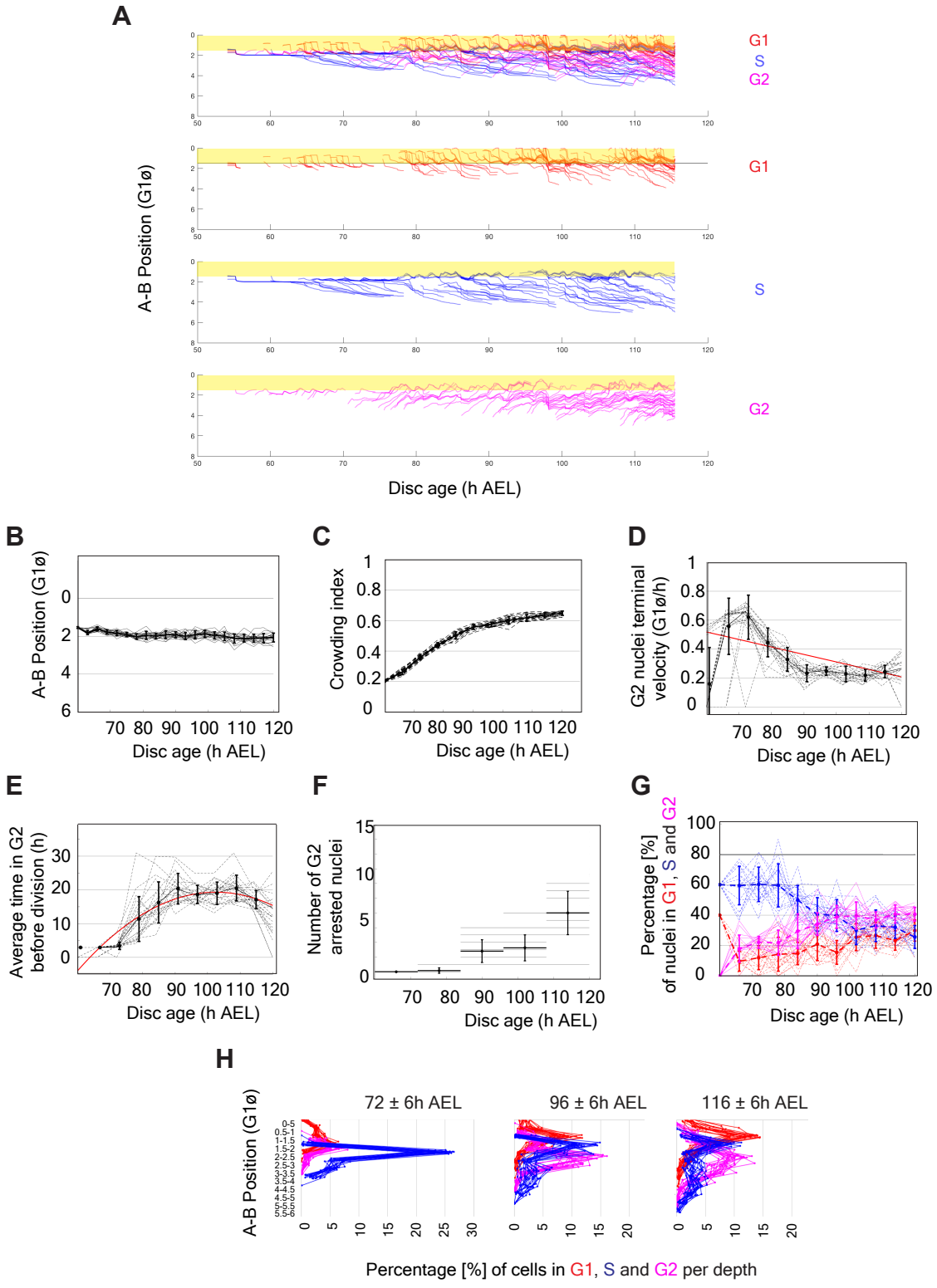
A
A-B Position (G1ø)
G1
S
G2
Disc age (h AEL)
B
A-B Position (G1ø)
Disc age (h AEL)
C
Crowding index
Disc age (h AEL)
D
G2 nuclei terminal velocity (G1ø/h)
Disc age (h AEL)
E
Average time in G2 before division (h)
Disc age (h AEL)
F
Number of G2 arrested nuclei
Disc age (h AEL)
G
Percentage [%] of nuclei in G1, S and G2
Disc age (h AEL)
H
A-B Position (G1ø)
72 ± 6h AEL
96 ± 6h AEL
116 ± 6h AEL
Percentage [%] of cells in G1, S and G2 per depth

Figure S2: Cell cycle phase analysis in simulated epithelia. Related to Figure 2. (A) Apical-basal position (G1∅) of individual nuclei G1 (red), S (blue) and G2 (magenta) over the course of a representative simulation. The yellow ribbon represents the mitotic zone where non-mitotic nuclei are excluded. Panels B-H show parameters for each of the 20 simulations performed: **(B)** average apical-basal position (G1∅) **(C)** average crowding index, **(D)** average terminal G2 velocity (G1∅/h) **(E)** average time spent in G2 before mitosis (h), **(F)** number of G2 arrested nuclei. **(G)** Percentage of nuclei in the different phases along time, and **(H)** nuclear distribution along apical-basal axis (G1∅), at 72 +- 6h, 96 +- 6h, and 116 +- 6h.

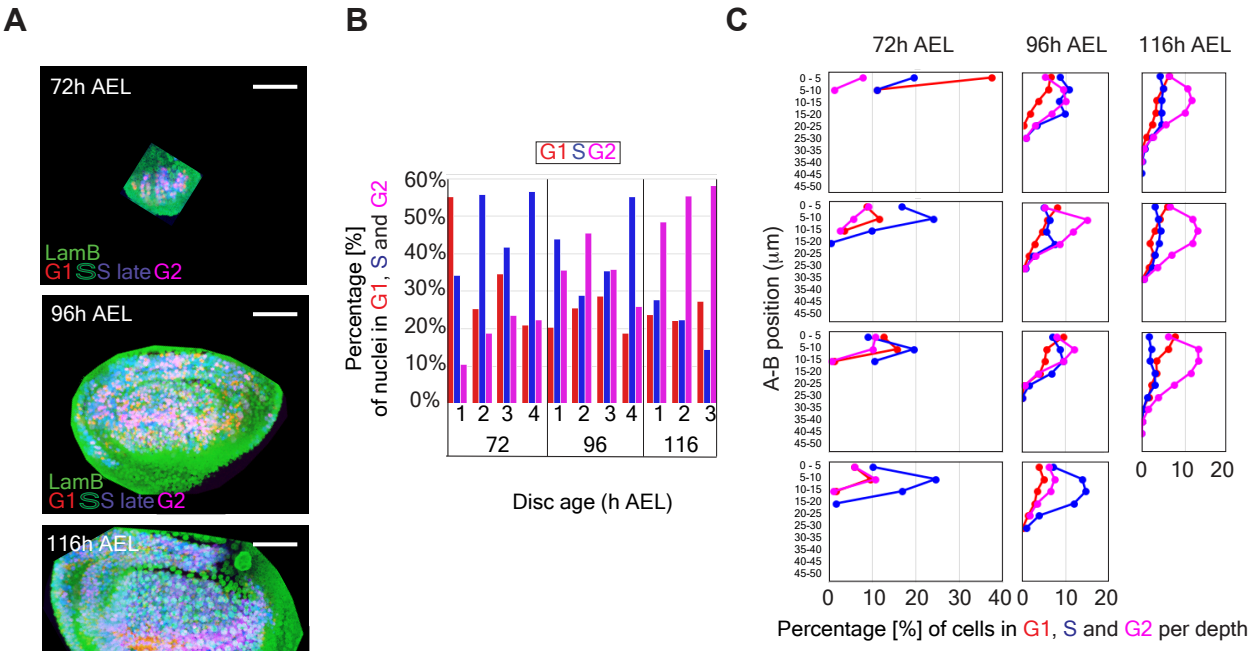
A
72h AEL
LamB
G1 S late G2
96h AEL
LamB
G1 S late G2
116h AEL
LamB
G1 S late G2
B
G1 S G2
Percentage [%] of nuclei in G1, S and G2
60%
50%
40%
30%
20%
10%
0%
1 2 3 4 1 2 3 4 1 2 3
72
96
116
Disc age (h AEL)
C
72h AEL
96h AEL
116h AEL
A-B position (µm)
0 - 5
5-10
10-15
15-20
20-25
25-30
30-35
35-40
40-45
45-50
0 10 20 30 40
0 10 20
0 10 20
Percentage [%] of cells in G1, S and G2 per depth

Figure S3: Spatio-temporal distribution of cell cycle phases in Drosophila wing imaginal discs. Related to Figure 3. (A) Max projection of wing imaginal discs expressing FUCCI (multiple colors) stained with anti-Lamin (Green). Nuclei in G1 appear in red, S appear either unmarked with FUCCI (still stained with the nuclear marker) or blue, and G2 appear in magenta. **(B)** Proportion of nuclei in the different phases for every disc analysed. 72h_disc1: 152 nuclei. 72h_disc2: 233 nuclei. 72h_disc3: 285 nuclei. 72h_disc4: 166 nuclei. 96h_disc1: 417 nuclei. 96h_disc2: 926 nuclei. 96h_disc3: 635 nuclei. 96h_disc4: 584 nuclei. 116h_disc1: 1892 nuclei. 116h_disc2: 1663 nuclei. 116h_disc3: 2334 nuclei. **(C)** Distribution of nuclei along apical-basal axis (μm) for every imaginal disc analysed.

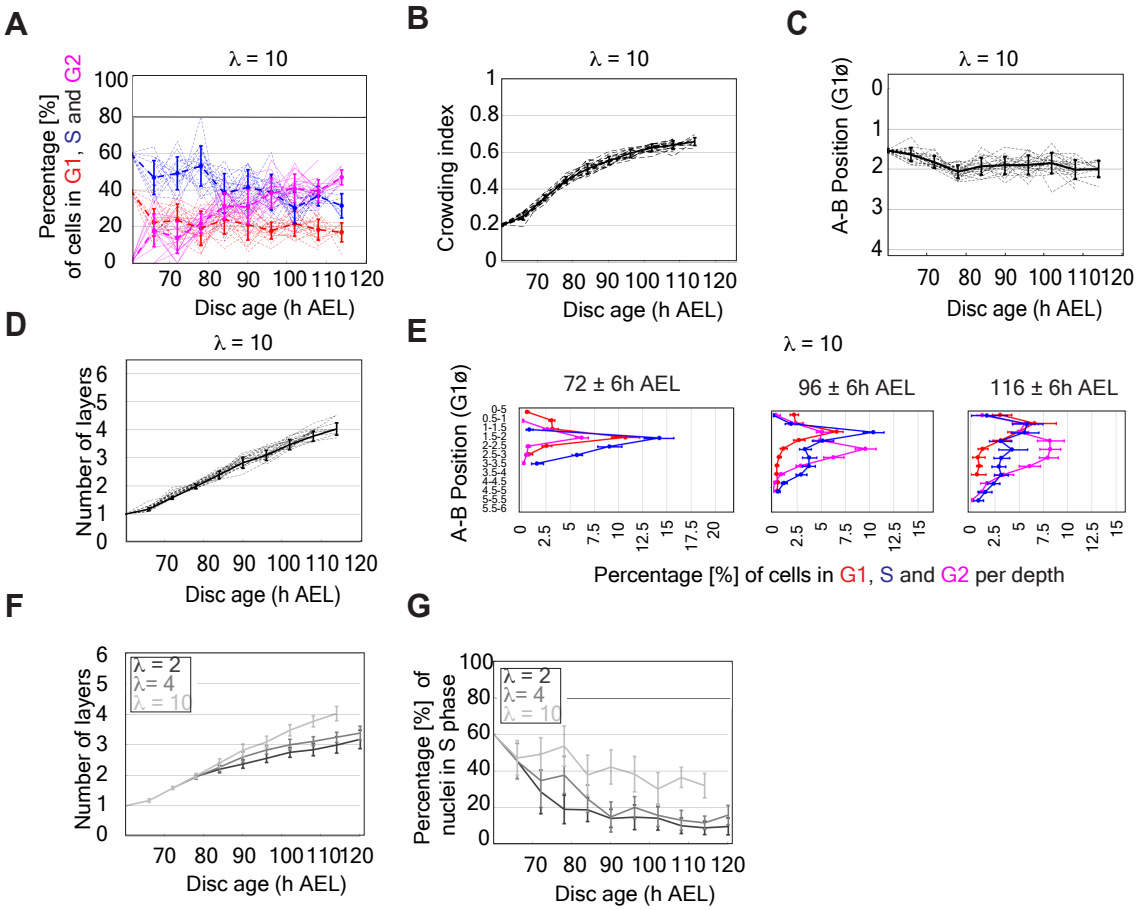
A
λ = 10
Percentage [%] of cells in G1, S and G2
Disc age (h AEL)
B
λ = 10
Crowding index
Disc age (h AEL)
C
λ = 10
A-B Position (G1ø)
Disc age (h AEL)
D
λ = 10
Number of layers
Disc age (h AEL)
E
λ = 10
72 ± 6h AEL
96 ± 6h AEL
116 ± 6h AEL
A-B Position (G1ø)
Percentage [%] of cells in G1, S and G2 per depth
F
λ = 2
λ= 4
λ = 10
Number of layers
Disc age (h AEL)
G
λ = 2
λ= 4
λ = 10
Percentage [%] of nuclei in S phase
Disc age (h AEL)

Figure S4: Computed spatio-temporal distribution of cell cycle phases and other parameters (multiple simulations). Related to Figure 4. For panels A-E, λ = 10, while panels F-G explore the effect of λ on nuclear behaviour. **(A)** Percentage of cells in the different phases of the cell cycle over time. **(B)** Average crowding index. **(C)** Average apical-basal position (G1∅). **(D)** Number of nuclear layers. **(E)** Distribution of cell cycle phases along the apical-basal axis (G1∅) at 72 +- 6h, 96 +- 6h and 116+- 6h AEL. **(F-G)** Increasing the range of the basal signal leads to an increased in the number of nuclear layers and a higher rate of proliferation (quantified by the percentage of nuclei in the S phase). The average of 20 simulations is represented in panels B, C, E, F and G. Error bars represent standard deviations.

ADDITIONAL REFERENCES

S1. Dye, N.A., Popovic, M., Iyer, K.V., Fuhrmann, J.F., Piscitello-Gomez, R., Eaton, S., and Julicher, F. (2021). Self-organized patterning of cell morphology via mechanosensitive feedback. Elife *10*. 10.7554/eLife.57964.

S2. Worley, M.I., Setiawan, L., and Hariharan, I.K. (2013). TIE-DYE: a combinatorial marking system to visualize and genetically manipulate clones during development in Drosophila melanogaster. Development *140*, 3275-3284. 10.1242/dev.096057.

S3. Neufeld, T.P., de la Cruz, A.F., Johnston, L.A., and Edgar, B.A. (1998). Coordination of growth and cell division in the Drosophila wing. Cell *93*, 1183-1193. 10.1016/s0092-8674(00)81462-2.

S4. Kirkland, N.J., Yuen, A.C., Tozluoglu, M., Hui, N., Paluch, E.K., and Mao, Y. (2020). Tissue Mechanics Regulate Mitotic Nuclear Dynamics during Epithelial Development. Curr Biol *30*, 2419-2432 e2414. 10.1016/j.cub.2020.04.041.

S5. Mirth, C.K., and Shingleton, A.W. (2012). Integrating body and organ size in Drosophila: recent advances and outstanding problems. Front Endocrinol (Lausanne) *3*, 49. 10.3389/fendo.2012.00049.

S6. Tozluoglu, M., Duda, M., Kirkland, N.J., Barrientos, R., Burden, J.J., Munoz, J.J., and Mao, Y. (2019). Planar Differential Growth Rates Initiate Precise Fold Positions in Complex Epithelia. Dev Cell *51*, 299-312 e294. 10.1016/j.devcel.2019.09.009.

S7. Mirth, C.K., Truman, J.W., and Riddiford, L.M. (2009). The ecdysone receptor controls the post-critical weight switch to nutrition-independent differentiation in Drosophila wing imaginal discs. Development *136*, 2345-2353. 10.1242/dev.032672.